



HAL
open science

Close-range remote sensing of Saturn's rings during Cassini's ring-grazing orbits and Grand Finale

Matthew Tiscareno, Philip Nicholson, Jeffrey N Cuzzi, Linda Spilker, Carl Murray, Matthew Hedman, Joshua Colwell, Joseph Burns, Shawn Brooks, Roger Clark, et al.

► **To cite this version:**

Matthew Tiscareno, Philip Nicholson, Jeffrey N Cuzzi, Linda Spilker, Carl Murray, et al.. Close-range remote sensing of Saturn's rings during Cassini's ring-grazing orbits and Grand Finale. *Science*, 2019, 364 (6445), pp.eaau1017. 10.1126/science.aau1017. insu-02615445

HAL Id: insu-02615445

<https://insu.hal.science/insu-02615445>

Submitted on 6 Aug 2020

HAL is a multi-disciplinary open access archive for the deposit and dissemination of scientific research documents, whether they are published or not. The documents may come from teaching and research institutions in France or abroad, or from public or private research centers.

L'archive ouverte pluridisciplinaire **HAL**, est destinée au dépôt et à la diffusion de documents scientifiques de niveau recherche, publiés ou non, émanant des établissements d'enseignement et de recherche français ou étrangers, des laboratoires publics ou privés.

Close-range remote sensing of Saturn's rings during Cassini's ring grazing orbits and grand finale

Matthew S. Tiscareno,^{1*} Philip D. Nicholson,² Jeffrey N. Cuzzi,³
Linda J. Spilker,⁴ Carl D. Murray,⁵ Matthew M. Hedman,⁶ Joshua E. Colwell,⁷
Joseph A. Burns,^{2,8} Shawn M. Brooks,⁴ Roger N. Clark,⁹ Nicholas J. Cooper,⁵
Estelle Deau,^{4,10} Cecile Ferrari,¹¹ Gianrico Filacchione,¹² Richard G. Jerousek,⁷
Stéphane Le Mouélic,¹³ Ryuji Morishima,^{4,10} Stu Pilorz,¹ Sébastien Rodriguez,¹¹
Mark R. Showalter,¹ Sarah V. Badman,¹⁴ Emily J. Baker,¹⁵
Bonnie J. Buratti,⁴ Kevin H. Baines,⁴ Christophe Sotin⁴

¹Carl Sagan Center for the Study of Life in the Universe, SETI Institute, Mountain View, CA 94043, USA

²Department of Astronomy, Cornell University, Ithaca, NY 14853, USA

³NASA Ames Research Center, Moffett Field, CA 94035, USA

⁴NASA Jet Propulsion Laboratory, California Institute of Technology, Pasadena, CA 91109, USA

⁵Astronomy Unit, Queen Mary University of London, London E1 4NS, UK

⁶Department of Physics, University of Idaho, Moscow, ID 83844, USA

⁷Department of Physics, University of Central Florida, Orlando, FL 32816, USA

⁸College of Engineering, Cornell University, Ithaca, NY 14853, USA

⁹Planetary Science Institute, Tucson, AZ 85719, USA

¹⁰Department of Earth, Planetary, and Space Sciences, University of California at Los Angeles,
Los Angeles, CA 90095, USA

¹¹Institut de Physique du Globe de Paris, Centre National de la Recherche
Scientifique (CNRS)-Unité Mixte de Recherche (UMR) 7154, Université Paris-Diderot,
Université Sorbonne-Paris-Cité (USPC), Paris, FRANCE

¹²INAF-IAPS (Istituto Nazionale di AstroFisica-Istituto di Astrofisica e Planetologia
Spaziali), Rome, ITALY

¹³Laboratoire de Planetologie et Geodynamique, CNRS-UMR 6112, Université de Nantes,
44322 Nantes, FRANCE

¹⁴Physics Department, Lancaster University, Lancaster LA1 4YB, UK

¹⁵Space Science Institute, Boulder, CO 80301, USA

*To whom correspondence should be addressed; E-mail: matt@seti.org

Saturn’s rings are an accessible exemplar of astrophysical disk processes, and a delicate tracer of the Saturn system’s dynamical processes and history. We present close-range remote sensing data of the main rings from the Cassini spacecraft. We find structures related to the detailed sculpting of rings by embedded masses, and evidence that impactors into the F ring are Saturn-orbiting streams of material. We find fine-scaled correlation in the B ring among optical depth and spectral properties and temperature, but anti-correlation in strong density waves in the A ring. We find a lack of spectral difference between plateaux and the rest of the C ring. We find sharply banded texture belts throughout the rings, and that the region outward of the Keeler gap is spectrally distinct from nearby regions. These results are likely related to radial stratification in particle properties, rather than in chemical composition.

Saturn’s main rings (1) are the regions known as the A, B, C, and F rings and the Cassini Division, which together constitute a broad dense disk of orbiting particles lying in the equatorial plane between 74,600 and 140,200 km (that is, 1.2 to 2.3 Saturn radii) from Saturn’s center. The normal optical depth (2) in the main rings is at least $\tau_n \gtrsim 0.1$, and in some locations $\tau_n \gg 1$. Particle composition is dominated by water ice, with trace contaminants, and particle size ranges from millimeters to meters (though a few localities, including the F ring, are rich in dust). By contrast, the dusty rings are inward (the D ring) and outward (the E and G rings) of the main rings, have $\tau_n \ll 0.1$, and are dominated by micron-sized particles (3).

The 13-year mission of the Cassini spacecraft at Saturn culminated in two stages. During the Ring Grazing Orbits (RGO), from December 2016 to April 2017, Cassini executed near-polar orbits that crossed the ring plane just outward of the F ring, providing close-range viewing of the outer portion of the main rings. During the Grand Finale (GF), from April to September 2017, the orbit shifted so closest approach to Saturn was inward of the D ring, passing a few

thousand km above Saturn’s cloud tops, providing close-range flybys of the inner portion of the main rings. We present and analyze optical remote sensing data taken during these flybys (4). We use data from Cassini’s Imaging Science Subsystem (ISS) (5), Visual and Infrared Mapping Spectrometer (VIMS) (6), Composite Infrared Spectrometer (CIRS) (7), and Ultraviolet Imaging Spectrograph (UVIS) (8).

Ring structure: Embedded moons and propellers

Each ring particle follows its own orbit around the planet. However, collective effects, including collisions and mutual self-gravity, affect the structure of the rings, as do interactions with larger orbiting objects. Moons ranging in size from Titan to Pan raise spiral density and bending waves in the ring (9–11). Moderate-sized moons Pan (radius $R \sim 14$ km) and Daphnis ($R \sim 4$ km) orbit within the outer part of the A ring and clear sharp-edged gaps (the Encke and Keeler gaps, respectively). Moons that are smaller than this, but still substantially larger than the largest continuum ring particles, create local disturbances that have been dubbed “propellers,” due to their shape (12).

Propellers are similar in principle to a circumferential gap like the Encke or Keeler gap, except that the embedded moon’s influence is overcome some distance downstream as the gap is filled in by the viscosity of the disk. Swarms of relatively small propellers, likely due to embedded moons ~ 100 m in size, are present in the Propeller Belts of the mid-A ring (13–15). There are probably more than 10^6 propellers over the several thousand km annulus of the Propeller Belts (15). Solitary larger propellers, likely due to embedded moons ~ 1 km in size, orbit beyond the Encke gap (16). At least a half-dozen of the latter have had their orbits tracked for the duration of the Cassini mission, and their shifting orbital attributes have been analyzed theoretically (12).

Among the science objectives of the RGO and GF (presented in Fig. 1) were close-range

flybys of Pan and Daphnis (17) and of three large propellers (namely, those nicknamed Blériot, Earhart, and Santos-Dumont), as well as high-resolution imaging of the Propeller Belts.

Daphnis and its vicinity: A false-color mosaic of Daphnis and its vicinity is shown in Fig. 1a. Daphnis itself is discussed in a companion paper (17); here we focus on the ring material perturbed by Daphnis. The image conveys the dichotomy in brightness and color that occurs at the Keeler gap (see below).

Immediately to the lower-left of Daphnis in Fig. 1a, within the gap, a strand of material is seen to follow a looping streamline. This material was likely pulled out of the sharp edge of the gap by a recent passage of Daphnis, and is now spreading along its streamline due to keplerian shear (18). Cassini was 13.5° above the ring plane when this image was taken, and the wavy edges of the Keeler gap are known to have a vertical component due to the orbital inclination of Daphnis (19), so the streamline seen here may be vertical and/or in-plane, which cannot be disentangled due to projection effects.

Downstream of Daphnis (which is trailing on the outer edge of the gap, but leading on the inner edge, due to keplerian shear), the edge is scalloped with a characteristic wavelength equal to $3\pi\Delta a$, where Δa is the difference in semimajor axis between Daphnis and the gap edge (12). It was previously known that the wavy edges due to Daphnis die away only a few wavecrests downstream, while those due to Pan in the edges of the Encke gap persist for the entire circumferential extent of the gap (20–22). Fig. 1a shows structure in the third wavecrest downstream of Daphnis. The trailing structure in the outer edge is seen on the left-hand side of Fig. 1a, and magnified in Fig. 1b. Macroscopic clumps of ring particles, which are not visible in the first or second wavecrest, dominate the third wavecrest, as the effects of Daphnis diminish. Furthermore, a gap or rift appears between the clump-studded wavecrest and the rest of the ring. We interpret this as a vertical feature: the ribbon of material may be rising above the ring plane, having been launched by the inclination of Daphnis, with the line of sight (due to

Cassini’s oblique viewing angle) passing through the vertical gap. As evidence for this, further downstream (in the left-hand portion of Fig. 1b), the same ribbon of material can be seen to pass behind the main portion of the ring, from Cassini’s point of view. This hypothesis does not exclude some degree of simultaneous radial structure in the third wavecrest. The difference in appearance between the third wavecrest and the first two may be partly due to a shroud of smaller particles (whose structure perhaps is primarily radial) that smooths the appearance of the first two wavecrests, which may have been absorbed into larger clumps in the third wavecrest.

The propeller belts: The propellers observed (13) in close-range images taken during Saturn orbit insertion (SOI), were substantially smaller than those seen in the Propeller Belts during the remainder of the Cassini mission (14, 15). Fig. 1c shows propellers of a similar size to those seen during SOI. We identified and analyzed 41 propellers in this image (4). We find a substantial range in propeller sizes, with the largest propellers being more than four times as large as the smallest (Table S1). We also find that the population density, average size, and size distribution may vary significantly with ring radius on finer scales than previously identified (Fig. S1), particularly in the vicinity of a moderately strong density wave. This implies that some combination of the parent bodies, subsequent evolution, and/or visibility of propellers is highly radially stratified.

Giant propellers: Close-range flyby images of propellers Blériot and Earhart are shown in Figs. 1d and 1e, respectively. Blériot was captured on the unlit side of the rings, where regions can be dark because of low optical depth (insufficient material to scatter sunlight towards the camera) or because optical depths are so high that the region is opaque. Earhart was captured on the lit side, where brightness usually increases monotonically as a function of optical depth. Additionally, close-range flybys captured images of propeller Santos-Dumont on both the lit and unlit sides of the rings, in images taken on both sides of ring-plane crossing during a single RGO pass (Fig. S2).

Complex structure is seen in all these images. The dark band through the center of Blériot, which is due to the disturbed region being opaque, extends further downstream than the similar dark band in the unlit-side image of Santos-Dumont, likely indicating higher surface mass densities.

Scalloping is present on the inner edges of the perturbed regions, analogous to patterns seen on the edges of the Encke and Keeler gaps. Equating the wavelength of the scalloping with $3\pi\Delta a$, and taking the full-width of the gap (i.e., twice Δa) to be $4\times$ the Hill radius r_H (23), where $r_H \equiv a(m/3M)^{1/3}$ for Saturn’s mass M and the central moon’s mass m and semimajor axis a , we calculate $\Delta a \simeq 2r_H$ to be 1.0 km for Santos-Dumont, and 1.6 km for Blériot.

The Hill radii imply masses of 7×10^{14} g for the central moon of Santos-Dumont, and 3×10^{15} g for that of Blériot. Most likely the actual size of each central moon is similar to its Hill radius (16), so that its bulk density is equal to the critical density for this region of the A ring, which is $\sim 0.4 \text{ g cm}^{-3}$ (24)), so that the above-calculated Δa approximates the triaxial moon’s longest axis.

The central propeller moon for each of these close-range propellers should be 2 – 3 pixels across in these images. However, we do not detect them, likely because they are obscured by the disturbed ring material swirling around them.

Ring structure: Texture belts

The main rings appear smooth in most images, though a clumpy straw-like texture has been identified in the troughs of strong density waves (25, 26). Other textures have been dimly perceptible in images throughout the Cassini mission, but have not been previously described or analyzed in any detail.

The RGO and GF images show several classes of ring texture, in well-defined radial bands, which do not correlate with other ring properties. Examples of these textures are shown in

Fig. 2.

There is growing evidence that some of the sharply-bounded features in the main rings are not due to changes in surface mass density, and thus must be due to variations in particle properties (27, 28). Composition, particle size, and regolith character (29) are candidate causes, though it is not clear how ring particles are sorted according to these properties. We find that these ring textures are localized into sharply defined radial bands (Fig. 2). We speculate that this may be due to differences in how ring particles bounce off each other when they collide, and thus might be correlated with regolith character (30).

Clumpy straw-like texture is seen not only in the troughs of strong density waves (Fig. 2a), but also in smaller waves such as those due to Prometheus (Fig. 2b) and at other types of locations. At 124,230 km from Saturn's center (in the inner A ring), a region characterized by fine-scale radial structure that is not well understood, a 100-km radial band exhibits clumpy structure while the regions around it do not (Fig. 2c). The clumpy texture at this location is correlated with a relatively bright band, but other relative brightness maxima nearby do not exhibit clumpy texture. The clumpy texture at this location is not associated with any spiral density wave, though such waves do occur at adjacent locations.

Many locations in the B ring (e.g., Fig. 2d) exhibit a more elongated texture. This streaky or feathery texture is often correlated with local minima in optical depths (though all optical depths are quite high in this region), which appear dark in lit-side images such as Fig. 2d. The landmark triple-humped belt in the outer Cassini Division also exhibits feathery texture (Fig. S3). Here the dark (gap-like) streaks are more discrete and may be related to features termed "ghosts" identified in UVIS occultations (31).

Another streaky texture appears in all 10 of the narrow and sharp-edged increases in brightness and optical depth in the C ring known as "plateaux." For example, Plateau P1 (Fig. 2e) exhibits streaky texture, while the non-plateau C ring material around it exhibits either clumpy

texture or no texture at all. Plateau P5 also exhibits streaky texture (Fig. S4). Their surface mass densities do not appear to be markedly different from those of the background C ring (32), so their defining characteristic must be related to particle properties (33).

An occultation of the star κ Orionis by the rings was observed using UVIS (4). Gaps $\gtrsim 20$ m across were seen in the plateaux, with an average separation of $0.5 - 1$ km. We modeled the plateaux with a simplified bi-modal transparency model using 19 UVIS stellar occultations (4). This model yields gap widths of $10 - 100$ m and vertical thicknesses of the plateaux of $10 - 40$ m. These average gap widths may represent the narrowest in a range of gap sizes, observable only with the high spatial resolution of the stellar occultations, with the dark streaks seen in the images being gaps on the wider end of the distribution.

Ring structure: F ring objects

Images of the F ring core obtained during the RGO and GF (Fig. 3) confirm the existence of a population of smaller objects by the detection of their associated mini-jets (34). While the core has an irregular, jagged shape (35, *their Fig. 4*), the population of mini-jets visible in Figs. 3d and 3e are all in phase, implying that they formed from a set of objects that collided with the core almost simultaneously. This observation suggests that, rather than representing a random population of small, colliding objects, the mini-jets in Figs. 3d and 3e had a common origin, probably as the result of a breakup of a single object. This supports previous inferences (36, 37) that impacts onto the rings may sometimes be due to Saturn-orbiting streams of material rather than to lone impacting objects. There is additional evidence for this in the Fig. 3b inset, where a collection of objects extending over $\sim 0.05^\circ$ (~ 100 km) appears to have recently emerged from the core. We interpret this feature as a more compact version of the multiple objects seen to cause the mini-jets in Figs. 3d and 3e. The calculated velocities (4) of $\sim 1.4 \text{ m s}^{-1}$ are consistent with those of previously-observed mini-jets (34).

We observe a narrow component in the F ring, 1 – 2 km in radial extent but perhaps unresolved, located ~ 10 km radially inward of the center of the bright core and visible in $\sim 50\%$ of Fig. 3a (i.e. extending over $\sim 2^\circ$). Although evidence for such a component has been seen before (35, *their Fig. 4h*), we infer from Fig. 3d that the original impact events that produced the mini-jet features in this part of the F ring originated when the source objects collided with the narrow component, implying the existence of substantial mass at this location. It has been suggested (38) that the true core of the F ring consists of discontinuous ring arcs, < 1 km in radial width, each extending over $\sim 2^\circ$ in longitude, wherein most of the F ring’s mass is contained. The observations in Fig. 3 do not constrain the mass of the F ring but they do provide supporting evidence for this interpretation and imply that the true core of the F ring may be radially offset from the brighter components that are more commonly seen.

Ring composition, particle size, and grain size

The reflectance spectrum of Saturn’s main rings in the ultraviolet (UV), visible, and near-infrared (IR) regions is dominated by fine-grained crystalline water ice with relatively small amounts of non-icy material (39, 40). The latter seems to consist of two distinct components. The first is responsible for the strong absorption at ultraviolet and blue wavelengths that gives the rings their pale tan or reddish color, and is now generally thought to be either organic in nature (41–43) or nano-phase particles of metallic iron or iron-oxides (44), while the second component is a spectrally-neutral absorber generally assumed to be silicates and/or carbon (45). Together, this icy mixture makes up the regolith coating the surfaces of the individual ring particles, whose sizes range from a few millimeters up to ~ 5 meters (39, 46–50).

The UV absorber appears to be present as inclusions within the individual grains of water ice (sometimes referred to as an intra-mix) and its abundance increases monotonically with proximity to Saturn (51–53). Its nature has been debated (54), though it is suspected to be a

primordial component of the rings. Recent observations and modeling (43) favor an organic material, perhaps tholins or mixtures of Polycyclic Aromatic Hydrocarbons (PAHs). Large organic molecules have been detected falling into Saturn's upper atmosphere (55), which may have come from the D ring. The neutral absorber, on the other hand, is inferred to be intimately mixed with the icy grains (i.e., as separate particles in close proximity, like a mixture of salt and pepper), and is most abundant in the optically-thin C ring and Cassini Division (52). It may be produced by the exposure of the originally-pure icy rings to bombardment by interplanetary debris (45).

Previous observations by Cassini have shown small-scale spatial variations in the main rings' visible and near-IR spectrum (51, 56). VIMS spectra have revealed that regolith grains are larger in the A and B rings; grain size and/or composition varies locally in the vicinity of strong density waves in the A ring and at several locations in the B and C rings (52, 53, 57). UVIS optical depth variance measurements have yielded similar conclusions about small-scale variations in the ring particle-size distribution (33).

Color and spectral variations: During the final orbits of the Cassini mission, high-resolution multi-color and spectral scans were taken across the entire ring system, covering both the lit and unlit sides of the rings (Figs. 4 and 5).

Color imaging with ISS was conducted at a resolution of $\sim 3 \text{ km px}^{-1}$, though this is a lower resolution than for the black-and-white images (e.g., Figs. 1 and 2). Fig. 4a displays a composite of true and enhanced color images (bottom two panels), with context given by a single unlit-face image (upper panel) in which darker bands are more optically thick. The pale tan color seen in the middle panel is generally not perceptible in a telescope, especially because Saturn is a yellowish tan itself (see below). Fig. 4b is an enhanced color composite from early in the Cassini mission, illustrating the different color outward of the Keeler Gap.

The observing mode for VIMS (4) resulted in a single, continuous image of the A, B, and

C rings (referred to as a noodle) 64 pixels wide by ~ 1000 pixels long. The spatial resolution ranges from $\sim 30 - 60 \text{ km px}^{-1}$, the gradient in resolution from one end of a noodle to the other being due to the changing spacecraft range. In the VIMS false color images shown in Fig. 5, the red channel corresponds to the center of a strong water ice absorption band, so reddish colors in the images signify less ice absorption, while the blue channel corresponds to a much weaker water ice band. The green channel is a continuum wavelength. The red color is most evident in the C ring and Cassini Division, but also in the extreme outer part of the A ring. The inner B ring also has slightly weaker ice bands than does the outer B or A rings (4).

Fig. 6 plots a set of standard spectral parameters for the main rings, derived from the VIMS lit-side scan on Rev 287 (58) and rebinned to a sampling interval of 20 km. Fig. 6a shows two representative brightness profiles of the rings at continuum wavelengths. Fig. 6c shows an optical depth profile of the rings for context, derived from a VIMS stellar occultation. In Fig. 6b are plotted water-ice band depths at 1.5 and 2.0 μm , calculated from the average spectrum for each radial bin (4). Also shown are spectral slopes in the visible portion of the spectrum, between 0.35 and 0.55 μm and between 0.55 and 0.85 μm (these are sometimes called the blue slope and the red slope, respectively, after the spectral regions where they are centered, rather than their shapes) Also plotted is the height of the 3.6 μm peak, which is defined by strong absorptions at 3 μm and $\sim 4.5 \mu\text{m}$, using the continuum level at 1.8 μm as a reference (4, 51, 52, 57).

As seen in previous work (51, 52), ice band depths are greatest in the outer half of the B ring and the outer two-thirds of the A ring, and lowest in the inner C ring and the Cassini Division. Band depths decrease smoothly from the middle A ring into the outer Cassini Division, and also from the innermost part of the B ring into the outer C ring, and then decrease further across the C ring. We confirm that regional transitions in band depths are gradual (51, 52), except we identify a more abrupt transition at the Keeler Gap (see below). More detailed views of portions

of Fig. 6 are shown in Figs. S9–S11.

Consistent with previous observations (51, 52, 57) we find that the fine-scale variations in the $0.35 - 0.55 \mu\text{m}$ slope and the IR water ice band depths in the A and B rings are well correlated. These curves exhibit very similar shapes down to the spatial resolution limit of the scans, and these parameters are more closely correlated with each other than either is with the ring brightness I/F (59). The $0.35\text{-}0.55 \mu\text{m}$ slope and ice bands show different behaviors within the lower optical depth C ring and Cassini Division, as well as across the transitions between those rings and the innermost B and A rings. Detailed spectro-photometric modeling of VIMS observations of the A, B, and C rings (40, 52) reveal that these varying trends can be attributed to a combination of variable particle regolith properties and compositions across the rings. For example, most of the fine-scale variations in the $0.35 - 0.55 \mu\text{m}$ slope and ice bands across the A and B rings can be attributed to shifts in grain sizes, while the deviations between these parameters in the lower optical depth C ring and Cassini Division are due to higher concentrations of darkening materials (neutral absorber) in those regions (40). After accounting for these variations, the differences between the overall trends across the inner B ring between the $0.35 - 0.55 \mu\text{m}$ slope and the ice band strengths could be due to an increase in the fractional abundances of the UV absorber closer to the planet (52).

While the $0.55 - 0.85 \mu\text{m}$ slope shows some of the same features in the A and B rings as the other spectral parameters, its overall behavior is quite different and so traces a different aspect of the rings' texture or composition. In particular, the $0.55 - 0.85 \mu\text{m}$ slope is elevated in the middle part of the C ring, which is consistent with evidence for enhanced silicate or carbon-rich material at that location inferred from radio wavelengths (60).

A ring: In the A ring, halos of reduced water-ice band depth around the strong density waves are seen in the VIMS observations. In Fig. S9 we plot the band depths in the A ring at a larger scale, together with profiles of the $0.35 - 0.55 \mu\text{m}$ and $0.55 - 0.85 \mu\text{m}$ slopes (though the latter

is fairly uniform in this region). Apart from the general inward decrease in band depths noted above, the most prominent features in the A ring profile are the peaks and dips seen at each of the strong density waves, especially those due to Janus. Centered on each of the Janus 4:3, 5:4 and 6:5 resonances there is a peak in all ice band-depths — and in the $0.35 - 0.55 \mu\text{m}$ spectral slope — symmetrically flanked by a region of reduced band depths. These features have been dubbed “halos” (51), from VIMS SOI data. The overall radial width of each halo is ~ 1000 km, which is much larger than the extent of the density waves associated with these resonances, and the halos are centered on the waves. The halo associated with the Mimas 5:3 resonance is less evident, even though it is one of the strongest density waves in the A ring. (the nearby Mimas 5:3 bending wave at 131,800 km shows neither peak nor halo in the band depth profiles.) Although the reason for the peaks and halos remains unclear, they may reflect an increase in the inter-particle collision rate within the density wave itself (exposing fresh, coarser-grained ice from deeper layers in the ring particles), accompanied by the ejection of debris that falls back onto the surrounding regions (which may reduce their mean grain size by spreading a cloud of small icy particles). UVIS optical depth variance results support this conclusion (33).

There are several ripples in the band depths and $0.35 - 0.55 \mu\text{m}$ slope in the innermost part of the A ring, inwards of 124,500 km. There are two moderately strong density waves in this region, due to the Pandora 5:4 and Prometheus 6:5 resonances, and the optical depth profile shows several sharp peaks in this neighborhood, but there is no correlation between the band depths and either the resonances or optical depth structure (61).

The region around and outward of the Keeler gap is less red, less backscattering, and has weaker ice bands than the rest of the A ring, as noted first in Voyager data (39, 62), and striking color variations are seen in early Cassini images such as Fig. 4b, where the color transition is very sharp and coincides with the location of the gap. In our observations, the spectral variations appear to start near 136,200 km and extend across the gap to the ring’s outer edge at 136,770 km.

They include decreases in both ice band depths and the $0.35 - 0.55 \mu\text{m}$ slope (Figs. 6 and S9), accompanied by an increase in the continuum brightness of the rings beyond the Keeler gap. This region is also known to have a lower surface mass density (63) and different particle-size properties (49, 50, 64) from the rest of the A ring.

It remains unknown whether the spectral difference of the trans-Keeler region implies a different composition and origin of the underlying material, or something else. Figs. 6b and S9 suggest weaker water ice bands in the trans-Keeler region. This may imply less water ice, and less of the accompanying organic reddening material. However, this hypothesis is difficult to reconcile with the relatively high reflectivity (I/F) in the same region, as seen in Figs. 6a and S9. A finer regolith grain size outside the Keeler gap could explain all three observations: flatter (less-red) visual wavelength spectra, higher I/F , and weaker ice bands, whether or not the material has an intrinsically different composition.

B ring: The B ring, the most opaque and massive of Saturn’s main rings (65), is conventionally divided into 4 or 5 sub-regions, based on varying structure and mean optical depth (66). The innermost or B1 region, between radii of 92,000 and 99,000 km, has a normal optical depth τ_n of 1 – 2 and is characterized by smooth, quasi-sinusoidal variations in τ_n and brightness with typical length scales of ~ 100 km (67). B1 is uniform in its spectral parameters (51), and in its optical colors (68, 69). Our VIMS data in Fig. 6 show very little variation in this region, except for a modest inward increase in both the $0.35 - 0.55 \mu\text{m}$ and $0.55 - 0.85 \mu\text{m}$ slopes and a slight drop in the ice band depths towards the C ring ramp over the innermost 500 km.

The B2 region is a zone of transition between the relatively low-optical-depth B1 region and the opaque B3 region (outward of 104,000 km) where $\tau_n > 3$ almost everywhere and frequently exceeds 5. The B2 region is characterized by a series of abrupt local transitions in τ_n , between a minimum of ~ 2 and a maximum of 5 or greater, at irregular intervals of 40–200 km. The VIMS data for this region (shown at a larger scale in Fig. S10) show a positive correlation between the

IR ice band depths, the $0.35 - 0.55 \mu\text{m}$ slope and τ_n , with every peak (or dip) in band depth being associated with a maximum (or minimum) in τ_n . At somewhat lower spatial resolution, a similar relationship between optical depth and ice band depths was previously demonstrated for the whole B ring (52); our data show that this correlation also holds down to the $50 - 100 \text{ km}$ scale in the B2 region. The correlation of optical depth with I/F is much weaker, with peaks in τ_n being associated with both maxima and minima in I/F in this region. This suggests that much of the I/F variations in the central B ring are due to variations in albedo and/or phase function rather than particle density — a conclusion previously drawn from Voyager imaging data (68).

Fig. 4a shows a high-resolution ISS color image, also of the B2 region. There are sharp boundaries between the discrete $\sim 100 \text{ km}$ wide bands in this region, which Cassini radio occultation data have shown to be even sharper than the ISS resolution (66). The narrow ringlets in the middle of this figure are about 40 km wide, while the broader bands near the right edge are $300 - 500 \text{ km}$ across. It remains unclear what causes the variable brightness of these ringlets and bands; the inherent reflectivity of the ring particle material, shadowing on their surfaces, their absolute abundance, and/or their packing density, may all play a role. The bottom panel of Fig. 4a is a color-enhanced version of the middle panel, in which blue colors indicate a “less red” or flatter spectrum at visible wavelengths than the redder colors, which mean a steeper-than-average spectrum. Observations by Voyager showed these color variations at lower resolution (68, 69); we find that that such well-defined color contrasts are sharply defined even down to the 3 km radial scale.

Across the very opaque B3 and B4 regions, between radii of $99,000$ and $115,000 \text{ km}$ (66), we find only small variations in the VIMS ice band depths or the $0.35 - 0.55 \mu\text{m}$ slope. A series of six low-amplitude oscillations in the band depths between $112,500$ and $114,200 \text{ km}$ are positively correlated with similar variations in both τ_n and I/F (52). Only within $\sim 1300 \text{ km}$

of the outer edge of the B ring is there a small but distinct decrease in all four of these spectral indicators, followed by an abrupt upturn in the final 500 km.

An exception to the generally flat band depths in this central part of the B ring is a broad but shallow dip in the ice band depths and $0.35 - 0.55 \mu\text{m}$ slope centered at 109,100 km and an even shallower dip centered at 107,400 km. These two features coincide with prominent peaks in I/F but with no obvious features in the optical depth profile. They may represent halos associated with the otherwise-invisible density waves that are expected to be driven by the Prometheus and Pandora 3:2 resonances (52), as seen in the A ring (Fig. S9). Both dips are located 500 – 600 km exterior to the actual resonance locations (52). Two similar shallow dips in the band depths are seen in the outermost part of the B ring, at 115,700 and 116,500 km, and bear a similar spatial relationship to the Enceladus 3:1 and Janus 3:2 resonances. This region is quite complex, with several other potentially interfering resonances due to Mimas and Prometheus (70).

C ring: Large-scale variations across the C ring visible in Fig. 6 include a steady inward decrease in IR band depths and the $0.35 - 0.55 \mu\text{m}$ slope parameter. On a finer scale, the most obvious structural features in the C ring are the plateaux. A typical plateau is ~ 150 km wide, with fairly abrupt edges and a peak optical depth of ~ 0.4 . They were detected in Voyager images (I) but are of unknown origin. Measurements of surface mass densities in the C ring (32) indicate that the plateau mass densities are similar to that of the adjacent background C ring ($\tau_n \simeq 0.1$), suggesting that their particle size distribution may be quite different (fewer particles in the meter-size range). VIMS observations at SOI yielded a marginal detection of variation in ice band depths between the plateaux and background regions (51). There is no discernible signature of the plateaux in the lit-side profiles of ice band depths, but there is a weak enhancement in the $0.35 - 0.55 \mu\text{m}$ slope parameter, which may be due to a local increase in the abundance of the UV absorber (52).

In the outer C ring (Fig. S11), the VIMS spectral data show that the $0.35 - 0.55 \mu\text{m}$ slope again tracks the depth of the ice band at $1.55 \mu\text{m}$, although the profiles for the C ring are noisier at visible wavelengths. These data show very little difference, if any, in spectral characteristics between the plateaux and the background. In several cases a very small increase in band depths within the plateaux may be detectable, at the level of 0.01 or 0.02, or 1.5–3%. These signatures are more apparent in the $0.35 - 0.55 \mu\text{m}$ slope than in any of the IR ice bands.

Correlation with optical depth: Color variations and spectral variations often imply compositional variations. However, this is not necessarily correct in Saturn’s rings. Fig. 4a shows that ring color correlates with optical depth down to the smallest scales discernible: optically thicker bands (darker in the top panel) are redder. A similar correlation between optical depth, ice band depths and spectral slope is visible in Fig. S9 and discussed above. The intrinsic composition is unlikely to vary in such a correlated way and on such small radial scales. Meteoroid bombardment spreads ejecta around the rings on 100 km radial scales, smoothing out any such variations (71). On the other hand, variable optical depth might lead to other local changes in ring particle and/or ring layer properties. Collisional dynamics in regions of varying optical depth can lead to varying volume or packing density of particles, which might affect the degree of multiple interparticle scattering. Multiple scattering is known to enhance spectral contrast and the ring material is red, so more multiple scattering can make a region redder and also increase the relative depths of absorption bands (72). The local packing density can also lead to nonclassical scattering effects (e.g., shadowing) which can affect the ring brightness as a function of particle albedo, also affecting spectral contrast (73). The frequency and/or speed of collisions may also vary between regions of different optical depth, and this constant jostling can affect the roughness, porosity, or grain size in the surfaces of the local particles (30, 52, 74, 75). Shadows on rough particle surfaces can change the particle phase function (76) in such a way as to exaggerate spectral contrasts at moderate to high phase angles. Monte Carlo models (4)

of scattering in closely-packed rings verified against similar models (40, 73, 77) suggest that the simplest explanation of the optical-depth-dependent reddening is increased multiple scattering in the optically thicker regions by the already reddish ring particles, given particle phase functions and surface reflectances like those of the ring particles (43), in the geometry of the observation (the ISS image in Fig. 4a was taken at a relatively high phase angle, defined as Sun-target-observer angle, of $\alpha = 110^\circ$). At shorter wavelengths, particle albedos are low enough that multiple scattering is minimal, leading to the variable reddening. So, the fine-scale color variations are consistent with a generally invariant composition, at least on 10 – 100 km lengthscales.

Ring temperature

CIRS measured the thermal emission from Saturn’s main rings – the A, B, and C rings, and the Cassini Division (7, 78, 79). During the Ring-Grazing orbits, CIRS obtained radial scans at spatial resolutions ranging from 260 – 470 km for the A ring to 660 – 930 km for the C ring for both their lit (northern) and unlit (southern) sides. Temperature T of the ring material were derived from spectra measured with focal plane 1 (FP1) between 10 and 600 cm^{-1} (17 μm to 1 mm) at a spectral resolution of 15 cm^{-1} . Rings were viewed nearly face-on for both the lit and unlit sides at absolute spacecraft elevation angles B (defined with respect to the ring plane) between 70° and 83° , and at phase angles of $\alpha \sim 60^\circ$ for the lit side and $\alpha \sim 120 - 130^\circ$ for the unlit side (Table S2). The representative ring temperatures and associated scaling factors were derived from Planck functions fitted to FP1 spectral data (80).

The lit-side temperatures varied from 80 to 100 K and the unlit-side temperatures varied from 70 to 90 K (Fig. 7). The radially-averaged ring temperatures were (C: 93 K, B: 85 K, CD: 88 K, A: 84 K) on the lit face and (C: 87 K, B: 73 K, CD: 80 K, A: 78 K) on the unlit face. Ring temperatures are driven by direct solar flux, solar flux reflected from Saturn, and Saturn

thermal flux, and depend on the transport of heat vertically through the rings via radiation, conduction, and particle transport. The flux due to Saturn-shine falls off approximately as the square of the distance from Saturn, and the Solar flux varies with the sine of the solar elevation angle above the ring plane. The optically thin C ring and Cassini Division are warmer than the optically thick A and B rings because incident flux from the Sun and Saturn penetrates through the ring, resulting in more efficient heating (81). The magnitudes of the thermal radiation emitted from the lit and unlit sides of the C ring and Cassini Division are consistent with the unlit side being in thermal equilibrium with the radiation field. That is not true of the B and A rings, where the unlit sides radiate at a much higher temperature than would be expected if they were in equilibrium with small amount of radiation that penetrates through the ring.

The heat transport within the C ring and Cassini Division are thought to be similar, though the C ring is always warmer than the Cassini Division due to its proximity to Saturn; similarly, the A and B ring temperatures are comparable, and at most epochs the lit B ring is warmer than the lit A ring due to their relative distances from Saturn. This Saturn-shine effect is at a minimum for the current data because at solstice the solar flux is large compared to the Saturn-shine, so that the lit A ring temperatures are comparable to those in the B ring. Details of the effect of Saturn-shine on the heating have been studied using the radial dependence of temperature at Saturn Equinox when solar flux is nearly zero (81), where the effect of reduced mutual shadowing between particles in the optically thinner rings could be modeled directly, given details of the incident flux.

Within each ring, the temperature difference between the lit and unlit face correlates to some extent with optical depth, although the actual magnitudes of the temperatures differ between rings. The correlations are shown graphically in Fig. S8, and discussed below with reference to Fig. 7. In the thick rings this effect has been noted before, and depends at least partially on efficiency of heat transport across the rings (82, 83). Detailed models indicate contributions

to these broad trends from a positive correlation between albedo and optical depth across the rings (84), of a nature consistent with preferential darkening of optically thinner rings due to meteoritic bombardment (45). The new observations at high spatial resolution show that, at finer scale, this correlation (of thermal gradient with optical depth) is not everywhere consistent, possibly due to local variations in ring structure and particle properties.

The temperature difference between the lit and unlit faces of the B ring correlates with optical depth, due mostly to variation on the unlit face. This could be caused by mutual collisions between particles in high optical depth regions hampering heat transport. Observational studies have shown that the thermal transmittance of the B ring correlates inversely with optical depth (82). Transport models of the B ring based on effective medium theory indicate that if heat transport by the vertical motion of particles is negligible, then the observed correlation of the ring thermal gradient with optical depth can be explained only if the increase in optical depth is due to a vertically thicker ring and not to a larger filling factor (83).

Fig. 7 indicates that in the A ring, the correlation of temperature differential with optical depth is consistent from the inner A ring to the flat outer regions, but there is a reverse in this trend in several locations where unlit-side temperatures of the A ring have local maxima correlating with the halos of the strongest density waves (Janus 4:3, 5:4, 6:5 and Mimas 5:3) and bending waves (Mimas 5:3). This decreases the temperature difference, even though the optical depths of these resonant locations are higher than the surrounding regions. This effect may be due to enhanced vertical heat transport or particle spin rates as a result of increased stirring of the ring particles in these regions. On the lit side of the rings, no temperature differences between the resonant locations and their surrounding regions are seen.

Correlations between temperature gradient and optical depth are not obvious in C ring and Cassini Division, partially due to the lower signal-to-noise in those regions. There appear to be dips in the unlit side temperature within at least the largest plateaux. In contrast to the B and

A rings where the lit side temperature varies little, there are features in the lit side temperature of the C ring, but these do not correlate well with the optical depth. The net result is that there is either a weak correlation or none between optical depth and temperature difference in the optically thin regions, and that other effects seem to be important here. Temperature maxima near the largest plateaux could be associated with mutual heating between particles (84), or could be associated with radial variations in particle properties or ring structure, the presence of which are hinted at by the streaky texture seen in images of the C ring plateaux.

Measurements by VIMS of the wavelength of the broad continuum peak around $\sim 3.6 \mu\text{m}$ can be used to infer the surface temperature of water ice. This method is applicable to ring particles, for which water ice is the dominant endmember (53). Spatial and temporal variations of the temperature as derived by this method are seen in the RGO and GF lit side data. For most of the A ring, this peak was found at about $3.58 \mu\text{m}$, corresponding to $T \sim 88 \text{ K}$, with lower temperatures in the outermost parts of the ring. The same temperature prevails inward to the mid-B ring, but increases to $T \sim 107 \text{ K}$ (peak at $3.60 \mu\text{m}$) in the inner B ring. In the C ring and Cassini Division, the $3.6 \mu\text{m}$ reflectance peak is faint and distorted by saturnshine, making temperature retrieval uncertain. However, data collected before the GF (53) have shown systematically higher temperatures; the inner C ring is 30 K warmer than the B ring, and the Cassini Division is 20 K warmer than the outer A ring. These VIMS results mirror the large-scale variations in mean albedo and optical depth, in the sense that the particles are colder where these quantities are higher. Furthermore, with the exception of the Cassini Division, the ring temperature decreases with distance from Saturn (53). However, the temperatures inferred by VIMS are generally higher than those measured by CIRS. Different depths to which ring particles are penetrated by the radiation measured by VIMS ($\sim 1 \text{ mm}$) and CIRS ($\gtrsim 10 \text{ mm}$) may play a role, as may the larger pixel footprint for CIRS, which could average warmer and cooler temperatures together.

Conclusion

We have reported imaging and spectral observations of Saturn’s rings taken during the final year of the Cassini mission. The rings are sculpted by embedded masses, producing structure visible down to our resolution limit. Correlations of spectral properties and temperature with optical depth is tight at many locations, while exceptions are found in certain regions already known to be enigmatic. Some spectral variations may be due to local variations in optical depth, rather than being solely due to particle composition or regolith grain size. Sharply stratified variations in particle properties, possibly including regolith character and bulk porosity as well as the distribution of particle sizes, likely play a role in producing many of the structures described here, and in some cases may supplant variations in surface mass density as the dominant effect.

References and Notes

1. J. N. Cuzzi, G. Filacchione, E. A. Marouf, *Planetary Ring Systems: Properties, Structure, and Evolution*, M. S. Tiscareno, C. D. Murray, eds. (Cambridge Univ. Press, 2018), pp. 51–92.
2. Optical depth τ quantifies the attenuation of a beam of light passing through the disk, measured in e -folding terms. That is, $\tau \equiv -\ln \mathcal{T}$ for the fractional transparency \mathcal{T} . The normal optical depth τ_n corrects for the effects of an inclined line of sight, thus approximating what the optical depth would be if the line of sight were normal to the ring plane (that is, if observed face-on to the rings).
3. M. M. Hedman, F. Postberg, D. P. Hamilton, S. Renner, H.-W. Hsu, *Planetary Ring Systems: Properties, Structure, and Evolution*, M. S. Tiscareno, C. D. Murray, eds. (Cambridge Univ. Press, 2018), pp. 308–337.

4. Materials and methods are available as supplementary material.
5. C. C. Porco, *et al.*, *Space Sci. Rev.* **115**, 363 (2004).
6. R. H. Brown, *et al.*, *Space Sci. Rev.* **115**, 111 (2004).
7. F. M. Flasar, *et al.*, *Space Sci. Rev.* **115**, 169 (2004).
8. J. E. Colwell, *et al.*, *Astron. J.* **140**, 1569 (2010).
9. P. Goldreich, S. Tremaine, *Ann. Rev. Astron. Astrophys.* **20**, 249 (1982).
10. F. H. Shu, *Planetary Rings*, R. Greenberg, A. Brahic, eds. (Univ. Arizona Press, Tucson, 1984), pp. 513–561.
11. M. S. Tiscareno, J. A. Burns, P. D. Nicholson, M. M. Hedman, C. C. Porco, *Icarus* **189**, 14 (2007).
12. F. Spahn, *et al.*, *Planetary Ring Systems: Properties, Structure, and Evolution*, M. S. Tiscareno, C. D. Murray, eds. (Cambridge Univ. Press, 2018), pp. 157–197.
13. M. S. Tiscareno, *et al.*, *Nature* **440**, 648 (2006).
14. M. Sremčević, *et al.*, *Nature* **449**, 1019 (2007).
15. M. S. Tiscareno, J. A. Burns, M. M. Hedman, C. C. Porco, *Astron. J.* **135**, 1083 (2008).
16. M. S. Tiscareno, *et al.*, *Astrophys. J. Lett.* **718**, L92 (2010).
17. B. Buratti *et al.*, (2018). *Science*, this issue.
18. Keplerian shear is the difference in orbital velocity between adjacent streamlines of ring material. For angular velocity n and radial distance a from Saturn's center, it is straightforward to differentiate Kepler's Third Law and obtain $dn/da = (3/2)(n/a)$.

19. J. W. Weiss, C. C. Porco, M. S. Tiscareno, *Astron. J.* **138**, 272 (2009).
20. M. S. Tiscareno, *et al.*, *AAS Division for Planetary Sciences Meeting Abstracts* **37**, 64.02 (2005).
21. P. A. Torrey, M. S. Tiscareno, J. A. Burns, C. C. Porco, *AAS Division on Dynamical Astronomy Meeting Abstracts* **39**, 15.19 (2008).
22. R. Tajeddine, P. D. Nicholson, M. S. Tiscareno, M. M. Hedman, J. A. Burns, *Icarus* **289**, 80 (2017).
23. M. Seiß, F. Spahn, M. Sremčević, H. Salo, *Geophys. Res. Lett.* **32**, L11205 (2005).
24. M. S. Tiscareno, M. M. Hedman, J. A. Burns, J. C. Castillo-Rogez, *Astrophys. J. Lett.* **765**, L28 (2013).
25. C. C. Porco, *et al.*, *Science* **307**, 1226 (2005).
26. M. C. Lewis, G. R. Stewart, *Icarus* **178**, 124 (2005).
27. M. S. Tiscareno, M. M. Hedman, J. A. Burns, J. W. Weiss, C. C. Porco, *Icarus* **224**, 201 (2013).
28. M. M. Hedman, P. D. Nicholson, *Astron. J.* **146**, 12 (2013).
29. Regolith is any layer of loose surface material.
30. E. Deau, *et al.*, *Icarus* **305**, 324 (2018).
31. K. Baillié, J. E. Colwell, L. W. Esposito, M. C. Lewis, *Astron. J.* **145**, 171 (2013).
32. M. M. Hedman, P. D. Nicholson, *Mon. Not. Roy. Astron. Soc.* **444**, 1369 (2014).
33. J. E. Colwell, L. W. Esposito, J. H. Cooney, *Icarus* **300**, 150 (2018).

34. N. O. Attree, C. D. Murray, G. A. Williams, N. J. Cooper, *Icarus* **227**, 56 (2014).
35. C. D. Murray, *et al.*, *Nature* **453**, 739 (2008).
36. M. S. Tiscareno, *et al.*, *Science* **340**, 460 (2013).
37. M. M. Hedman, J. A. Burns, M. R. Showalter, *Icarus* **248**, 137 (2015).
38. J. N. Cuzzi, *et al.*, *Icarus* **232**, 157 (2014).
39. J. Cuzzi, *et al.*, *Saturn from Cassini-Huygens*, M. Dougherty, L. Esposito, S. M. Krimigis, eds. (Springer-Verlag, Dordrecht, 2009), pp. 459–509.
40. M. Ciarniello, *et al.*, *Icarus* **317**, 242 (2019).
41. F. Poulet, J. N. Cuzzi, *Icarus* **160**, 350 (2002).
42. F. Poulet, D. P. Cruikshank, J. N. Cuzzi, T. L. Roush, R. G. French, *Astron. Astrophys.* **412**, 305 (2003).
43. J. N. Cuzzi, *et al.*, *Icarus* **309**, 363 (2018).
44. R. N. Clark, *et al.*, *Icarus* **218**, 831 (2012).
45. J. N. Cuzzi, P. R. Estrada, *Icarus* **132**, 1 (1998).
46. E. A. Marouf, G. L. Tyler, H. A. Zebker, R. A. Simpson, V. R. Eshleman, *Icarus* **54**, 189 (1983).
47. H. A. Zebker, E. A. Marouf, G. L. Tyler, *Icarus* **64**, 531 (1985).
48. R. G. French, P. D. Nicholson, *Icarus* **145**, 502 (2000).
49. R. A. Harbison, P. D. Nicholson, M. M. Hedman, *Icarus* **226**, 1225 (2013).

50. T. M. Becker, J. E. Colwell, L. W. Esposito, A. D. Bratcher, *Icarus* **279**, 20 (2016).
51. P. D. Nicholson, *et al.*, *Icarus* **193**, 182 (2008).
52. M. M. Hedman, *et al.*, *Icarus* **223**, 105 (2013).
53. G. Filacchione, *et al.*, *Icarus* **241**, 45 (2014).
54. J. N. Cuzzi, *et al.*, *Science* **327**, 1470 (2010).
55. J. H. Waite, *et al.*, *Science* **362**, aat2382 (2018).
56. R. H. Brown, *et al.*, *Astron. Astrophys.* **446**, 707 (2006).
57. G. Filacchione, *et al.*, *Icarus* **220**, 1064 (2012).
58. The Rev code is a three-digit label for Cassini's orbits around Saturn. For operational reasons, Saturn orbit insertion (SOI) was followed by Revs 00A, 00B, and 00C, and then by Revs 003 through 293.
59. I/F is a measure of the observed brightness I as normalized by a perfect Lambert surface's reflection of the incident solar flux πF .
60. Z. Zhang, *et al.*, *Icarus* **281**, 297 (2017).
61. The sharp peak at 123,570 km in both τ_n and I/F is probably associated with the Prometheus resonance.
62. L. Dones, J. N. Cuzzi, M. R. Showalter, *Icarus* **105**, 184 (1993).
63. M. S. Tiscareno, B. E. Harris, *Icarus* **312**, 157 (2018).
64. R. G. Jerousek, J. E. Colwell, L. W. Esposito, P. D. Nicholson, M. M. Hedman, *Icarus* **279**, 36 (2016).

65. L. Iess et al., (2018). *Science*, this issue.
66. J. E. Colwell, *et al.*, *Saturn from Cassini-Huygens*, M. Dougherty, L. Esposito, S. M. Krimigis, eds. (Springer-Verlag, Dordrecht, 2009), pp. 375–412.
67. L. J. Horn, J. N. Cuzzi, *Icarus* **119**, 285 (1996).
68. P. R. Estrada, J. N. Cuzzi, *Icarus* **122**, 251 (1996).
69. P. R. Estrada, J. N. Cuzzi, M. R. Showalter, *Icarus* **166**, 212 (2003).
70. M. M. Hedman, P. D. Nicholson, *Icarus* **279**, 109 (2016).
71. P. R. Estrada, R. H. Durisen, J. N. Cuzzi, D. A. Morgan, *Icarus* **252**, 415 (2015).
72. F. Poulet, J. N. Cuzzi, D. P. Cruikshank, T. Roush, C. M. Dalle Ore, *Icarus* **160**, 313 (2002).
73. H. Salo, R. G. French, *Icarus* **210**, 785 (2010).
74. E. Deau, *et al.*, *Icarus* **226**, 591 (2013).
75. E. Deau, *Icarus* **253**, 311 (2015).
76. J. N. Cuzzi, L. B. Chambers, A. R. Hendrix, *Icarus* **289**, 281 (2017).
77. C. C. Porco, *et al.*, *Astron. J.* **136**, 2172 (2008).
78. V. G. Kunde, *et al.*, *Proc. SPIE Vol. 2803, Cassini/Huygens: A mission to the Saturnian systems*, L. Horn, ed. (SPIE, Bellinsham, 1996), pp. 162–177.
79. D. E. Jennings, *et al.*, *Applied Optics* **56**, 5274 (2017).
80. L. J. Spilker, *et al.*, *Planet. Space Sci.* **54**, 1167 (2006).

81. L. Spilker, C. Ferrari, R. Morishima, *Icarus* **226**, 316 (2013).
82. S. Pilorz, N. Altobelli, J. Colwell, M. Showalter, *Icarus* **254**, 157 (2015).
83. E. Reffet, M. Verdier, C. Ferrari, *Icarus* **254**, 276 (2015).
84. R. Morishima, *et al.*, *Icarus* **210**, 330 (2010).
85. N. J. Cooper, C. D. Murray, G. A. Williams, *Astron. J.* **145**, 161 (2013).
86. C. D. Murray, R. S. French, *Planetary Ring Systems: Properties, Structure, and Evolution*, M. S. Tiscareno, C. D. Murray, eds. (Cambridge Univ. Press, 2018), pp. 338–362.
87. K. Beurle, *et al.*, *Astrophys. J. Lett.* **718**, L176 (2010).
88. J. E. Colwell, L. W. Esposito, M. Sremčević, *Geophys. Res. Lett.* **33**, L07201 (2006).
89. J. E. Colwell, L. W. Esposito, M. Sremčević, G. R. Stewart, W. E. McClintock, *Icarus* **190**, 127 (2007).
90. The standard VIMS instantaneous field of view (equivalent to a pixel for an optical imager) subtends a solid angle of 0.5×0.5 mrad. In IR-high-resolution mode this is reduced to 0.25×0.5 mrad, with the smaller dimension in the VIMS fast-scan direction used in LINE mode.
91. This description applies to the instrument's IR channel which employs a 1D detector array to obtain 256 simultaneous spectral measurements for each spatial pixel; the visible channel uses a CCD detector to obtain an entire line of pixels at 96 wavelengths simultaneously ('push-broom' mode). In LINE mode, the two channels are synchronized so that a full line of IR pixels is observed while the VIS channel does a single integration.
92. RC-19 calibration file, http://atmos.nmsu.edu/data_and_services/atmospheres_data/Cassini/vims.html.

93. J. W. Boardman, F. A. Kruse, *10th Thematic Conference on Geologic Remote Sensing* (Ann Arbor, 1994), pp. 407–418.
94. C. H. Acton, *Planet. Space Sci.* **44**, 65 (1996).
95. R. G. French, *et al.*, *Icarus* **103**, 163 (1993).
96. R. N. Clark, T. L. Roush, *J. Geophys. Res.* **89**, 6329 (1984).
97. R. N. Clark, P. G. Lucey, *J. Geophys. Res.* **89**, 6341 (1984).
98. R. Morishima, H. Salo, *Icarus* **181**, 272 (2006).
99. L. J. Spilker, *et al.*, *Icarus* **171**, 372 (2004).
100. D. L. Gresh, P. A. Rosen, G. L. Tyler, J. J. Lissauer, *Icarus* **68**, 481 (1986).
101. **Acknowledgements:** We thank the Cassini project, the science planners, and the instrument teams for making these observations possible. We thank Tilmann Denk for the color mosaic image processing that created Fig. 1a. **Funding:** MST acknowledges funding from the NASA Cassini Data Analysis program (NNX16AI33G) and the Cassini project. The work of LJS, SMB, ED, and RM was carried out at the Jet Propulsion Laboratory, California Institute of Technology, under contract with NASA: government sponsorship acknowledged. CDM and NJC thank the Science and Technology Facilities Council of the UK (Grant No. ST/P000622/1) for financial support. **Author contributions:** MST, PDN, JNC, LJS, CDM, MMH, and JEC took the lead in executing and analyzing the observations. JAB, SMB, RNC, NJC, ED, CF, GF, RGJ, SLM, RM, SP, SR, and MRS contributed to the same. SVB, EJB, BJB, KHB, and CS contributed to executing the observations. **Competing interests:** The authors declare no competing interests. **Data and materials**

availability: All Cassini data are publicly available from the NASA Planetary Data System. For browsing, go to <https://pds-rings.seti.org/viewmaster/volumes> . For search, go to <https://tools.pds-rings.seti.org/opus> .

Supplementary Materials:

Materials and Methods

Supplemental Text

Figs. S1 to S11

Tables S1 to S4

References (85–100)

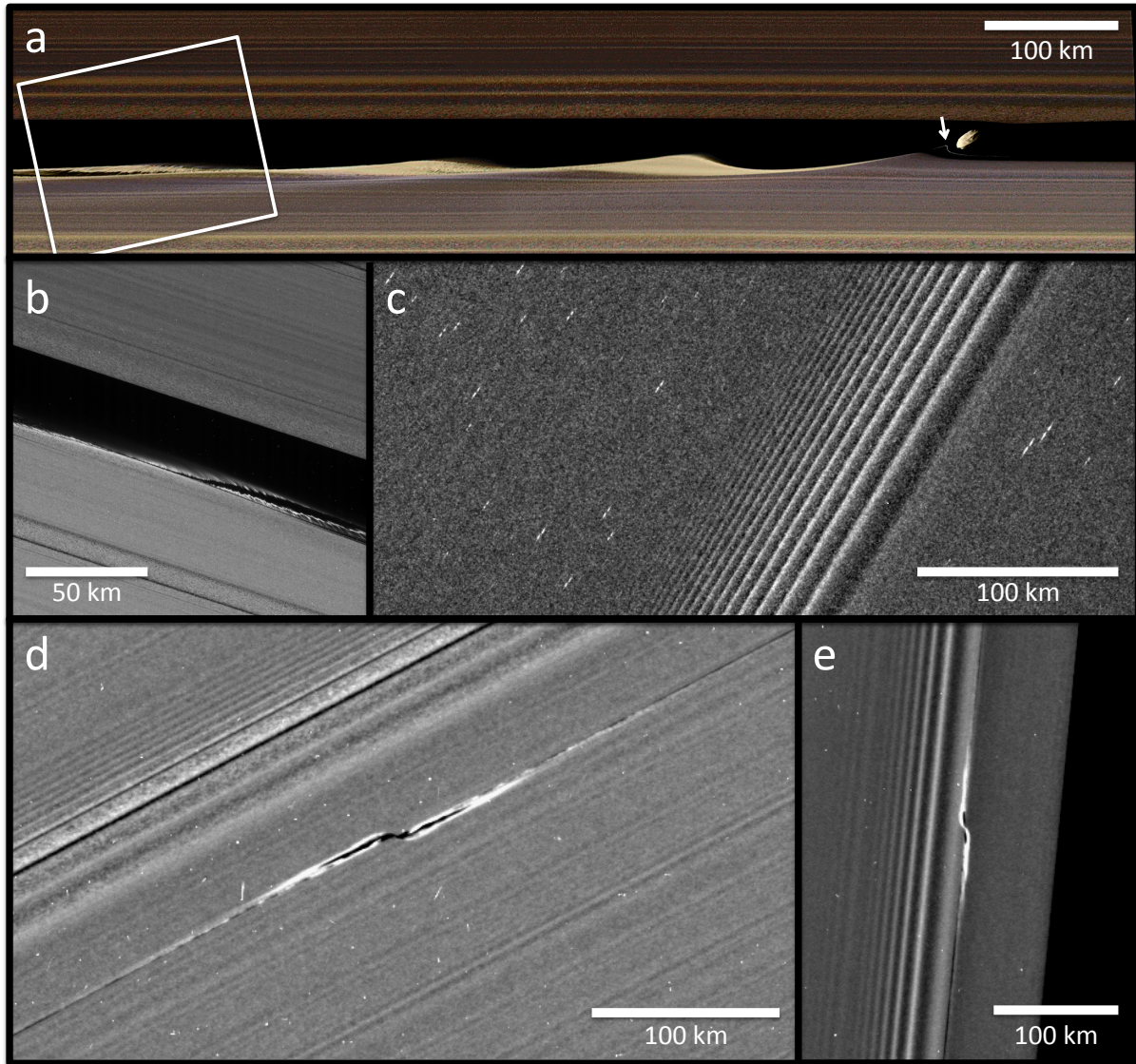


Figure 1: **Embedded moons cause structure in the main rings.** (a) False-color image mosaic (4) showing Daphnis in the Keeler gap on the lit side of the rings, with three wavecrests of the structure raised by Daphnis in the gap's outer edge. Each successive wavecrest from right-to-left is older, having elapsed an additional orbital period (~ 13 hr) since its close approach to Daphnis. The direction to Saturn is up, and the orbital direction is to the right. A thin strand of material (indicated by arrow) is present in the gap to the lower-left of Daphnis, and there is intricate structure in the third wavecrest downstream. The box on the left-hand side indicates the approximate footprint of the image in panel b. (b) A further closeup of the third wavecrest, on the unlit side of the rings. (c) Propellers in the Propeller Belts of the mid-A ring on the unlit side of the rings. The large multi-banded structure across the center of the panel is the Prometheus 9:8 spiral density wave. (d) The propeller Blériot on the unlit side of the rings. (e) The propeller Earhart on the lit side of the rings.

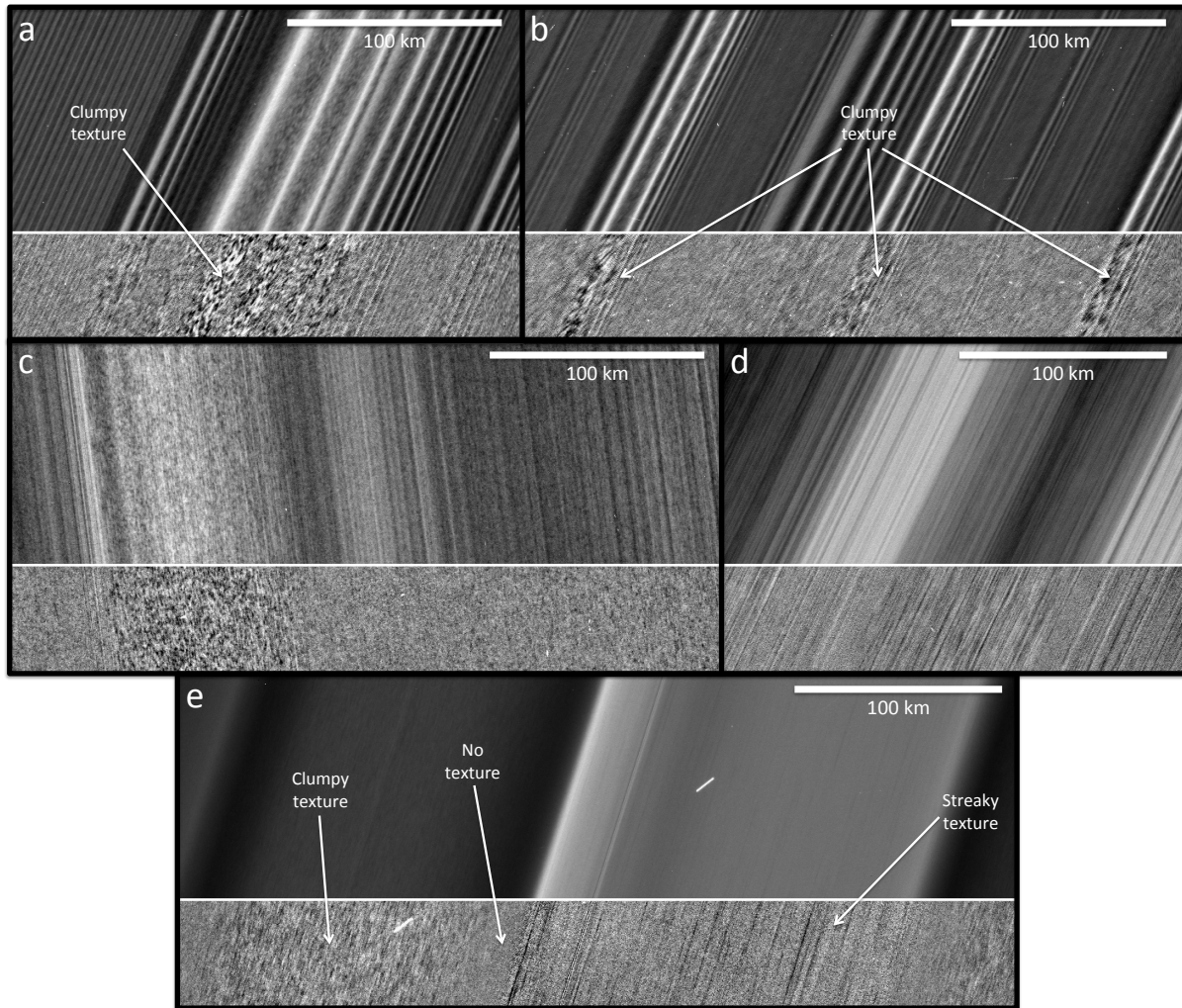


Figure 2: **Belts of textures in the main rings.** A strip along the bottom of every panel has been filtered by subtracting the average radial profile of the image, so that local structures and textures are more visible. All images in this figure show the lit side of the rings (4). (a) Straw-like clumps in the troughs of the strong Janus 6:5 density wave in the outer A ring. (b) Straw in the troughs of the Prometheus 26:25, 27:26, and 28:27 density waves (left-to-right) in the outer A ring. (c) Straw-like texture in one radial band of the inner A ring but not surrounding regions. (d) Feathery texture in some radial bands of the outer B ring (especially those with lower brightness in the main part of the image) but not surrounding regions. (e) Plateau P1 and its environs in the C ring, with three different textures in close proximity to each other.

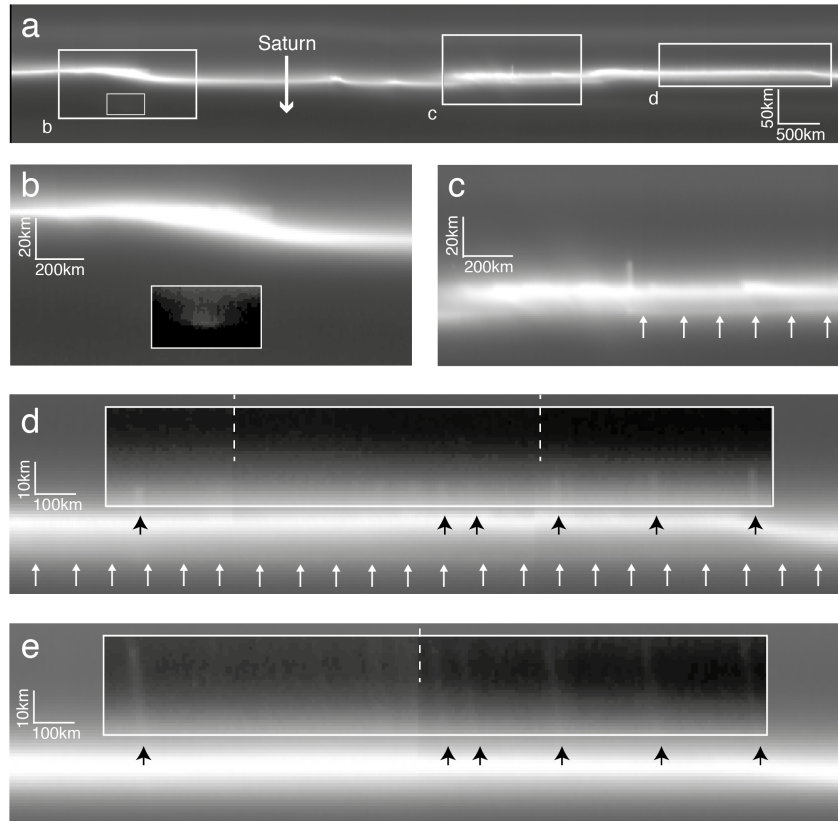


Figure 3: **Mini-jets and other structures in the F ring.** A high resolution mosaic (4) of the F ring core region showing evidence for a population of small objects, their evolution, and a possible narrow component. (a) Context mosaic. White boxes indicate the regions shown in the other panels. (b) Enlarged portion of panel (a), showing a linear feature near the core with a contrast-enhanced inset showing a faint, linear feature below it. (c) Enlarged portion of panel (a), showing a mini-jet emerging ~ 10 km from the core with evidence of a narrow ring component parallel to and below the core. There is also evidence of a fan-shaped structure (4) to the left, characteristic of an embedded object on an eccentric orbit. (d) Enlarged portion of panel (a), with a region immediately above the core (indicated by the white rectangle) selectively contrast enhanced to bring out faint features. Several mini-jets (black arrows) emerge from the core, leaving trails that extend between ~ 7 km (left) and ~ 14 km (right) from the core. There is also evidence that the mini-jets originate in a narrow ring component parallel to the core but ~ 10 km below it (white arrows). (e) Same as panel (d), except portion of a different image mosaic of the same region, taken 85 minutes later. Although the resolution is poorer, the evolution of the mini-jets is evident, having doubled in length and undergone Keplerian shear. The dashed lines in (d) and (e) indicate longitudes where adjacent images overlap, leading to the production of slight offsets in the mosaics. The white arrows on (c) and (d) indicate the location of the narrow component.

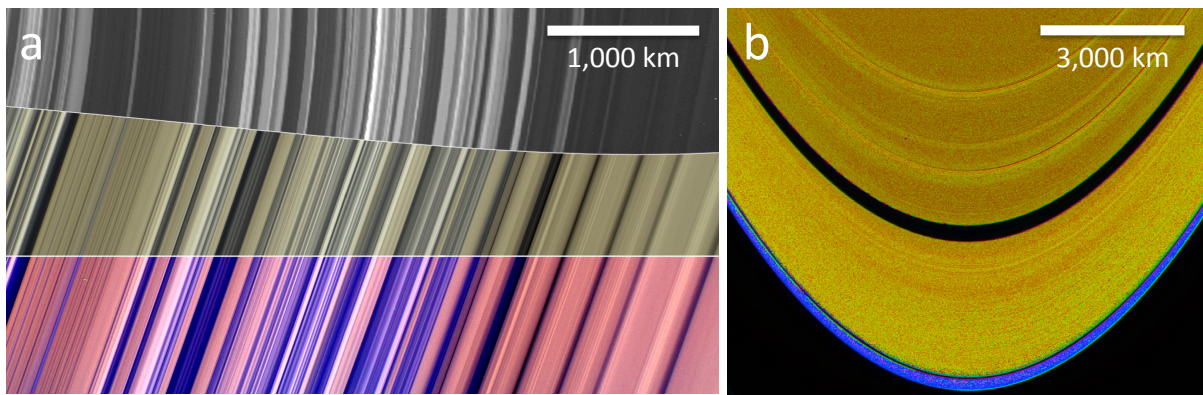


Figure 4: **Color images of the B and A rings.** (a) The inner-central B Ring, covering the region from 98600 to 105500 km from Saturn's center at about 3 km px^{-1} . The top panel is a context image in black-and-white, while the middle and bottom panels are (respectively) true-color and enhanced-color versions. (b) The mid- and outer-A ring (4). Fig. S10 shows the same region, as observed by VIMS.

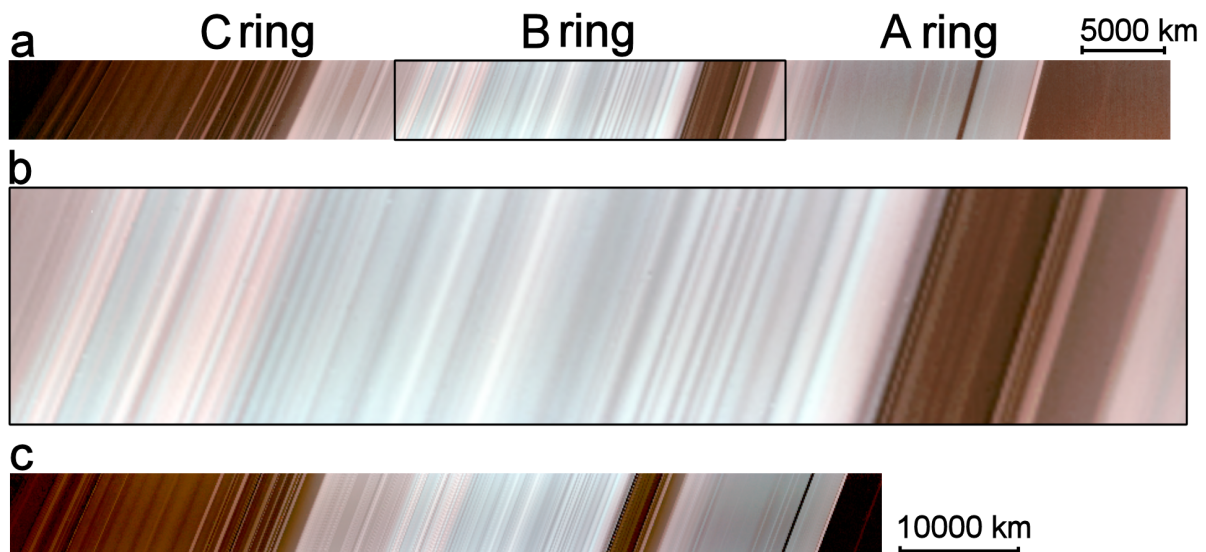


Figure 5: **Near-IR spectral scans.** VIMS radial scans across the lit side of the main rings, displayed as false-color images. (a) The scan obtained on Rev 262, on 21 February 2017. (b) An enlarged view of the outer 2/3 of the B ring, and Cassini Division. (c) The scan obtained on Rev 287, on 7 August 2017. The scale bars indicate the average radial scale for each scan, though in both cases the true scale varies across the scan due to the varying projected radial velocity of the spacecraft. On Rev 262 the velocity was a maximum in the B ring and the radial scale is compressed there by $\sim 15\%$. On Rev 287, the velocity decreased from right-to-left by $\sim 30\%$ and the scale in the C ring is correspondingly stretched out.

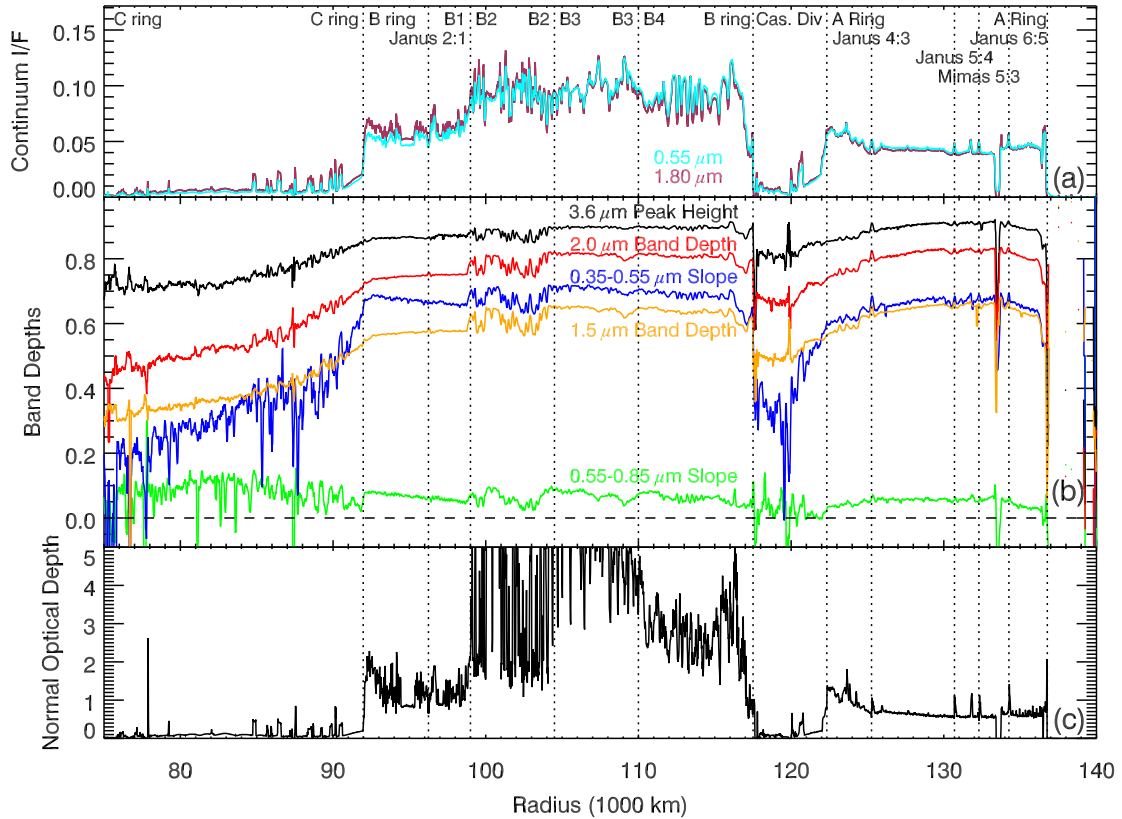


Figure 6: **Radial profiles of spectral parameters.** Data shown here are from the VIMS lit-side scan on Rev 287. Vertical dotted lines indicate (as labeled) the locations of density waves or of boundaries between ring regions including the A, B, and C rings and the B ring subregions B1 through B4. (a) Reflectivity of the rings at continuum wavelengths of 0.55 and 1.8 μm , with the locations of major ring boundaries and the strongest density waves identified by vertical dotted lines. (b) Fractional depths of the water ice bands at 1.55, 2.0 and 3.6 μm in orange, red, and black, respectively, as well as the 0.35 – 0.55 μm and 0.55 – 0.85 μm slopes in green and blue (see text for definitions). (c) Optical depth profile of the rings obtained from a VIMS occultation of the star γ Crucis on Rev 082 (52, 70). Versions of this figure that zoom on the A, mid-B, and outer-C rings (respectively) are included as Figs. S9, S10, and S11.

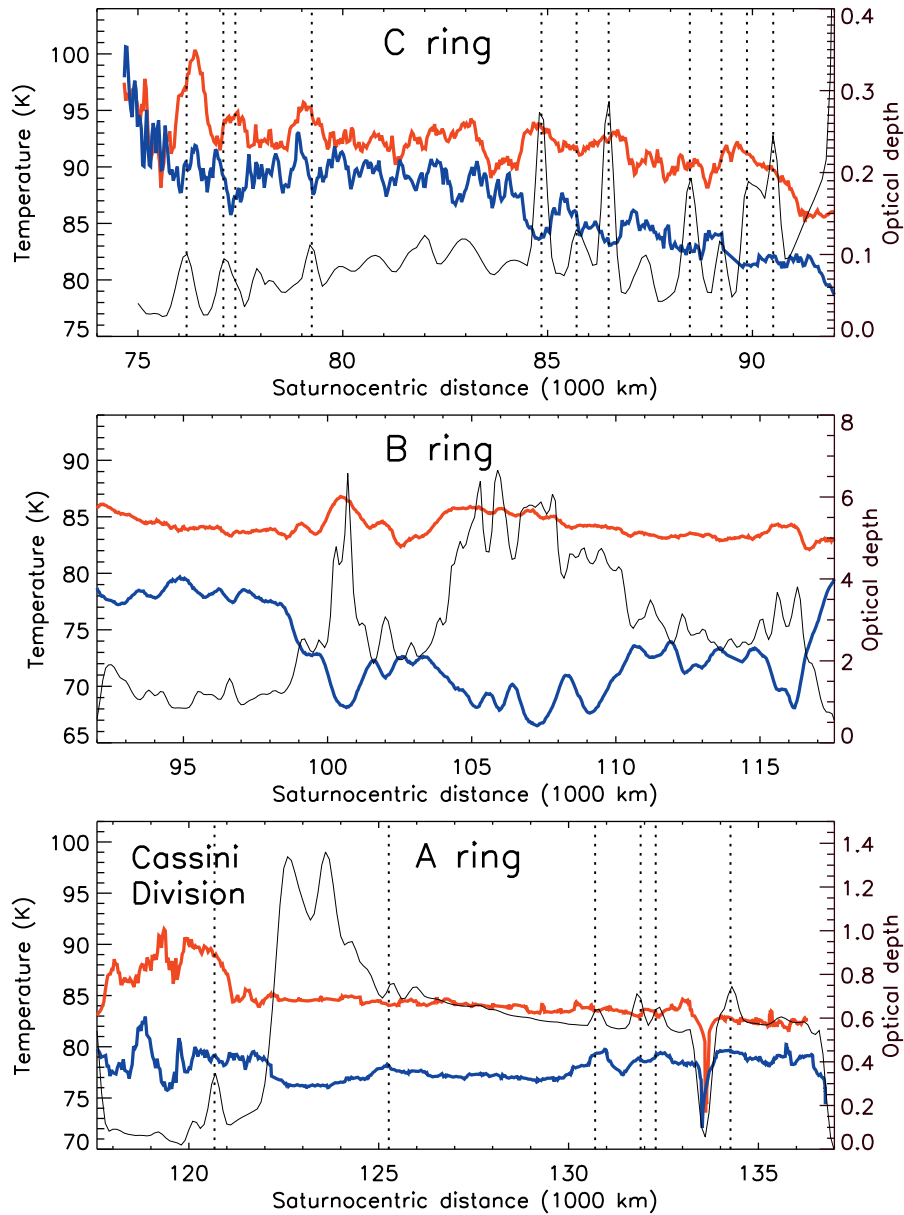


Figure 7: **Radial temperature profiles.** Observations by CIRS of the lit (red) and unlit (blue) faces of (a) the C ring, (b) the B ring, and (c) the Cassini division and the A ring. The black curve shows, for context, the optical depth measured by Cassini UVIS (8) and smoothed over a radial extent comparable to the typical CIRS footprint size. The vertical dotted lines show locations of prominent features: the plateaux in the C ring and the Cassini Division and the density and bending waves in the A ring (Table S3).



Supplementary Materials for

Close-range remote sensing of Saturn's rings during Cassini's ring grazing orbits and grand finale

Matthew S. Tiscareno,^{1*} Philip D. Nicholson,² Jeffrey N. Cuzzi,³ Linda J. Spilker,⁴
Carl D. Murray,⁵ Matthew M. Hedman,⁶ Joshua E. Colwell,⁷ Joseph A. Burns,^{2,8}
Shawn M. Brooks,⁴ Roger N. Clark,⁹ Nicholas J. Cooper,⁵ Estelle Deau,^{4,10} Cecile Ferrari,¹¹
Gianrico Filacchione,¹² Richard G. Jerousek,⁷ Stéphane Le Mouélic,¹³ Ryuji Morishima,^{4,10}
Stu Pilorz,¹ Sébastien Rodriguez,¹¹ Mark R. Showalter,¹ Sarah V. Badman,¹⁴
Emily J. Baker,¹⁵ Bonnie J. Buratti,⁴ Kevin H. Baines,⁴ Christophe Sotin⁴

Correspondence to: matt@seti.org

This PDF file includes:

Materials and Methods
Supplementary Text
Figs. S1 to S11
Tables S1 to S4

Materials and Methods

Observation details

Dates with form YYYY-DDD are in day-of-year (DOY) format, in which days are numbered sequentially rather than being cited by month. Observation times are given in Coordinated Universal Time (UTC).

ISS images were calibrated using the CISSCAL software package (5), which is available from the NASA Planetary Data System at <https://pds-rings.seti.org/cassini/iss/software.html>

The ISS instrument had two components, a Narrow Angle Camera (NAC) and a Wide Angle Camera (WAC).

The color mosaic shown in Fig. 1a was created by combining images from the Rev 257 DAPHNIS observation. Colors obtained at lower resolution were overlaid onto higher-resolution black-and-white images. The colors derive from the IR3, Green, and UV3 filters on Cassini's ISS camera, so Fig. 1a is not a true-color image but rather enhanced color.

Observation details for the remainder of Fig. 1 are as follows: (b) Image N1863268347, at 0.16 km px^{-1} . (c) A portion of image N1871322544, at 0.39 km px^{-1} . (d) A portion of image N1870702753, at 0.50 km px^{-1} . (e) A portion of image N1868838859, at 0.67 km px^{-1} .

Observation details for Fig. 2 are as follows: (a) Image N1870075955, at 0.52 km px^{-1} . (b) Image N1870076370, at 0.47 km px^{-1} . (c) Image N1866983227, at 0.41 km px^{-1} . (d) Image N1862643689, at 0.63 km px^{-1} . (e) Image N1875233884, at 0.33 km px^{-1} .

Figs. 3a through 3d have resolution $\sim 1.05 \text{ km px}^{-1}$ in the radial direction, while Fig. 3e has resolution $\sim 1.60 \text{ km px}^{-1}$ in the radial direction. The context mosaic (Fig. 3a) covers 4° of longitude ($\sim 10,000 \text{ km}$) and is composed of 13 ISS NAC images obtained on 2017 July 13. The radial width is 200 km.

The images in Fig. 4a are from the HRESCOLBC mosaic taken by the Cassini Imaging Science Subsystem (ISS) during Rev 282, on 2017-187 (July 6, 2017), with phase angle $\alpha = 109^\circ$, solar elevation angle $B' = 26.7^\circ$, and spacecraft elevation angle $B = 35^\circ$. The middle panel of Fig. 4a is a near-true-color set, constructed from Cassini's Red, Green, and Blue filters.

Figure 4b shows a three-color composite from the observation RADCOLOR, taken during Rev 00A on 2004-298 (October 24, 2004). The radial resolution at the ring ansa is 13 km px^{-1} . The phase angle $\alpha = 48^\circ$, solar elevation angle $B' = -23.6^\circ$, and spacecraft elevation angle $B = -7.5^\circ$, looking at the lit face. The specific images used were N1477310577(RED), N1477310627(GRN), and N1477310544 (BL1). The images were calibrated and geometrically corrected with the standard CISSCAL code to I/F , converted to tiff format, and aligned by hand as (respectively) RGB channels in Photoshop, with subsequent adjustments made to accentuate relative color contrast.

In Fig. 5, the false-color coding is red = $2.02 \text{ }\mu\text{m}$, green = $1.78 \text{ }\mu\text{m}$ and blue = $1.27 \text{ }\mu\text{m}$. Further details are as follows: (a) This image from Rev 262 is 935 by 64 pixels in size, with an average radial spacing in the horizontal direction of 76 km. The data were acquired at a spacecraft elevation angle of $B \sim 71^\circ$ and a fixed phase angle of $\alpha = 62^\circ$. The local hour angle varied from ~ 10 to ~ 12 h. (c) This image from Rev 287 is 708 by 64 pixels in size, with an average radial spacing between vertical lines of 95 km. The data were acquired at a spacecraft elevation angle of $B \sim 80^\circ$ and a fixed phase angle of $\alpha = 73^\circ$. The local hour angle ranged from ~ 3 h in the A ring, at the start of the scan, to ~ 6 h in the C ring at its end.

The data in Fig. 6a have been rebinned to a uniform sampling resolution of 20 km. The data in Fig. 6b have been smoothed to a resolution of 100 km. The context profile in Fig. 6c has been binned to 10 km resolution.

Processing and modelling for images of the main rings

A radial profile can be derived from an image by azimuthally averaging pixels that fall within radial bins (11, 63). For Figs. 2, S3, and S4, a radial profile was combined with the geometry of the image to create a filter that was then subtracted from the image to obtain a version emphasizing azimuthal and compact structures. This radially filtered image is shown below the unfiltered image (included for context).

The 41 propellers identified in image N1871322544 (Fig. 1c) were fitted to a pair of offset two-dimensional gaussians according to a model that has been described previously (15). Results are listed in Table S1 and plotted in Fig. S1. The center of the model structure is given in terms of both image coordinates (line and sample, which are respectively the vertical and horizontal coordinates in pixels, as measured from the image’s top-left corner) and the radius and longitude within the ring plane. The azimuthal and radial dimensions of the fitted two-dimensional gaussians are a and b , respectively. The azimuthal and radial offsets between the centers of the fitted two-dimensional gaussians are $\Delta\ell$ and Δr , respectively.

Processing and modelling for images of the F ring

The mosaics in Figs. 3a through 3d are derived from the observation HIRESAFRG001 in Rev 283, obtained on 2017 July 13. The original sequence consisted of 81 NAC images using clear filters, each with an exposure duration of 1.2 s, covering 24.7° degrees of co-rotating longitude (based on an F ring mean motion of $581.96^\circ/\text{d}$ with an epoch of 2007 January 1 at 12:00 UTC). The mean longitudinal coverage of each image was 0.43° . Each image was reprojected with respect to an F ring core model (85, *their Table 3, Fit 11*). The final scale was $0.003^\circ \text{ px}^{-1}$ in longitude and 1 km px^{-1} in radius. The mosaic in Fig. 3a was cropped to show only the region between co-rotating longitudes 271.5° at the left and 275.5° at the right, covering 13 images. The radial extent is 200 km centered on the approximate location of the core and increasing in radius from the planet in the vertical direction. In Fig. 3a the faint ring

above the core and almost parallel to it is a sheared jet resulting from a collision elsewhere in the core. There is another, fainter sheared jet below the core and angled to it, meeting the core at approximately the location of the disturbed region shown in Fig. 3b. There is longitudinal smearing of 1 – 2 pixels in this mosaic.

Fig. 3b is an enlargement of a region ($\sim 0.67^\circ$ by 100 km) to the left of the main mosaic with a selected, inset enhancement highlighting a longitudinal feature $\sim 0.05^\circ$ (~ 100 km) in extent located ~ 55 km below the core, interpreted to contain a set of objects that have just collided with the F ring core. The enhancement also shows evidence of faint material connecting these objects to the core region. This is similar to previously observed structures (35) and complex mini-jets (34).

Fig. 3c is an enlargement of a section ($\sim 0.67^\circ$ by 100 km) of the core to the right of center. It shows a prominent mini-jet extending ~ 10 km from the outer edge of the core. The mini-jet itself seems to originate from a narrow ring component that appears to be parallel to the core but ~ 10 km closer to the planet. Left of the mini-jet is evidence for a faint fan structure extending over $\sim 0.3^\circ$ indicative of the presence of an embedded object on an orbit with a relative eccentricity with respect to the core (35, *their Fig. 3*; 86, *their Fig. 13.29*).

Fig. 3d is an enhanced enlargement of a section ($\sim 0.83^\circ$ by 60 km) at the right side of the mosaic. As with Fig. 3c, there is some evidence of a narrow component parallel to the core but below it. Several mini-jets protruding from the outer edge of the core extend by radial distances from the core edge ranging from ~ 7 km (at the left) to ~ 14 km (at the right). The mini-jets themselves may originate at the location of the narrow component, located ~ 10 km from the core closer to the planet. We interpret the objects forming the synchronised mini-jets to be made from loose agglomerations of material brought together under the perturbing effect of Prometheus (87). Prometheus and collisions with the core can also play a role in disrupting these objects but, to a first approximation, the disrupted pieces will maintain orbits close to their

original ones with perhaps small changes in semi-major axis leading to the constituent particles drifting with respect to one another. This in turn leads to the appearance of objects following similar trajectories as they cross the core.

Fig. 3e is an enhanced enlargement of a section ($\sim 0.83^\circ$ by 60 km) produced from images in the same observation, HIRESAFRG001 in Rev 283, but taken ~ 85 min after the mosaic shown in Figs. 3a through 3d. The full mosaic consisted of 41 NAC ISS images covering approximately the same range of co-rotating longitude. The mean longitudinal coverage of each image was 0.66° . A subset of 9 images covering co-rotating longitudes between 271.5° and 275.5° was taken and then a section of that was then used for a direct comparison with the core shown in Fig. 3d. Although the resolution is worse (1.60 km/pixel in the radial direction compared with 1.05 km px^{-1} in the original) it is sufficient to see that the same mini-jets can be identified and their orbital evolution observed. All mini-jet features have approximately doubled in length and undergone keplerian shear making them lean towards the left (lower co-rotating longitudes). The calculated velocities of $\sim 1.4 \text{ m s}^{-1}$ are consistent with those of the previously-described mini-jets (34). A similar lengthening and shearing process is seen to occur to the prominent mini-jet originally seen in Fig. 3c. It is not possible to resolve the narrow ring component in any section of the later mosaic.

The velocities of the mini-jets in the radial direction were calculated by measuring the radial distances covered in the 85-minute time interval between the detections shown in Figs. 3d and 3e, each of which consists of a radial reprojection. This provides no information about azimuthal velocities.

Monte Carlo models of scattering in closely-packed rings

We have made a preliminary assessment as to which of the various possibilities is the most plausible cause of the correlation of ring color with local optical depth, which is observed all the

way down to the resolution limit of a few km (Fig. 4a). To do this, we have used Monte Carlo ray tracing models of nonclassical, closely-spaced particles with realistic size distributions. This technique has been described previously (40, 73). It has been tested thoroughly against classical results in the limit where they should be valid, namely low optical depth and volume density (45). It has also been validated against published models (73) in the nonclassical regime of high optical depth and volume density, where there is no closed-form solution. Rather than assuming an isotropic (Lambertian) phase function as in previous work, we employ a particle roughness/shadowing parameter S , which parameterizes the phase function and albedo of the particles. The operation of this parameter has been described previously (76). Fig. S6 shows that, for the viewing geometry of Fig. 4a, multiple scattering increases with optical depth and with particle reflectance, for all values of S .

Fig. S6 shows the ratio $R_{I/F}$ of total ring I/F (that is, reflectivity) to the single scattering component,

$$R_{I/F} = \frac{(I/F)_{\text{total}}}{(I/F)_{\text{ss}}} \quad (\text{S1})$$

where $(I/F)_{\text{total}}$ is the total ring I/F and $(I/F)_{\text{ss}}$ is the single-scattering component of the I/F , for four different values of S . The multiple scattering contribution is thus $(R_{I/F} - 1)$ times as large as the singly-scattered contribution. This is all we need for a preliminary assessment, since Fig. S6 shows that all particle roughnesses share a common qualitative behavior. At this moderately high phase angle, the figure shows the multiple scattering contribution increasing dramatically with increasing normal reflectance of the particle surfaces; the effect is also stronger at higher optical depths. The effect of local volume density D is smaller than the optical depth or particle reflectance effects. This shows the importance of multiple scattering for optical depths in the range found in the observed part of the rings, in this illumination and viewing geometry. Since the individual particles are reddish (40, 43), the reflectance is higher at long wavelengths, so the multiple scattering contribution is also higher at long wavelengths

and optical-depth dependent (the $\tau = 3$ curves are higher than $\tau = 1$ curves). That is to say, at high particle reflectance, the ring brightness is optical depth dependent. However, at short wavelengths the particle reflectance is known to be low (40, 43); in this regime there is little or no optical depth dependence of ring brightness. The consequence is that the rings become more red as optical depth increases, at this part of the rings and in this geometry. This explains the observations more naturally than other possible explanations.

Observations and modelling for UVIS occultations

The streaks seen in high-resolution ISS images of Plateau P1 are elongated and aligned to the direction of orbital motion. In order to better understand this texture, we analyzed all 31 of the Cassini UVIS stellar occultations with $B < 35^\circ$. For an occultation, the angle of the observer's line of sight with respect to the ring plane is equal to both the stellar elevation angle B' and the spacecraft elevation angle B . In our data set, B ranges from 1.2° to 32.1° . The clock angle ϕ for these occultations, which is the orientation of the star's projected track on the ring plane with respect to the radial direction, ranged from $\phi = 3^\circ - 316^\circ$. We compared the normal optical depth τ_n measured by these occultations to those computed using a self-gravity wake model (88, 89). This model treats the ring as consisting of alternating regions of high and low optical depth aligned to the direction of orbital motion ($\phi = 90^\circ$) as seen in the ISS images. We constrain the gap optical depth to be no greater than 0.01, based on the dark appearance of the streaks on both the lit and unlit faces of the ring. The 31 optical depth profiles were binned to 10 km radial resolution to give average optical depths spanning many clumps and gaps at each viewing geometry. We modeled the ring using infinitely-long rectangular slabs separated by nearly empty gaps and found the best-fitting parameters by ray-tracing through the model ring and matching optical depths. Model computed optical depths fit well with a reduced chi-squared less than a homogenous ring model.

Derivation of ring temperatures

We excluded CIRS spectra with ratio of the angular displacement of the boresight during the signal integration to the angular size of the footprint > 0.5 , to avoid smeared data. To increase the signal-to-noise ratio, 10 nearby spectra were averaged for each pointing. The loss of the spatial resolution due to the averaging process remains small, because the radial extent of 10 nearby pointings is smaller than each footprint size in most cases. The ring spectrum I_ν as a function of wave number ν is assumed to take the form of

$$I_\nu = \beta B_\nu(T), \quad (\text{S2})$$

where β is a scaling factor incorporating the filling factor and the effective emissivity of the ring structure (Fig. S7), $B_\nu(T)$ is the wavenumber-dependent Planck function, and T is the representative ring temperature. The temperature T and the scaling factor β are simultaneously derived by minimizing χ^2 (80). The spectral data between 50 and 450 cm^{-1} (200 μm to 22 μm , which covers the blackbody peaks for all temperatures likely to occur within Saturn's rings) are used for the fitting. To see correlation/anti-correlation of ring temperatures with ring optical depth, a standard radial optical depth profile (a UVIS-measured occultation of the star β Centauri, (8)) was smoothed over the typical CIRS FP1 footprint size (84).

The observational geometries of radial scans are summarized in Table S2. For the C ring, the B ring, and the Cassini division, we use the radial scans (L262 and U262) taken on 2017-052 for both the lit and unlit sides. For the A ring, we use the radial scans (L268 and U268) taken on DOY 95 in 2017 for both the lit and unlit sides. The scans L268 and U268, although they cover only outer main rings, have spatial resolutions higher than those for L262 and U262 by a factor of ~ 2 . The observational geometries of two scans are similar to each other for each side of rings. Since the ring opening angles during these observations were very close to the maximum value given by the obliquity of Saturn, 26.73° , the ring temperature at each

observational geometry (e.g. phase angle) was also near a maximum for the mission.

Observation design and data processing for VIMS images

Observation design: Observations were made of the sunlit rings on RGO Revs 255 and 262 and on GF Rev 287, in each case starting at ~ 4 h before periapse (P) and ending at $P - 1$ h. The unlit side of the rings was observed on RGO Revs 260 and 262, starting at $P + 1$ h and continuing for 2.5 hrs. In each case, the instrument stared in a fixed inertial direction while the motion of the spacecraft carried the field of view across the rings, resulting in a single, continuous image (referred to as a ‘noodle’). The viewing direction was within 20° of normal to the ring plane for all five observations, in contrast to the relatively low values of B of the SOI observations (41), yielding a phase angle of $\alpha \sim 65^\circ$ for the sunlit rings and $\sim 130^\circ$ for the unlit rings. Table S4 lists the relevant geometric and instrumental parameters for each observation.

On Rev 262, the aim point moved outwards from the inner edge of the C ring to the F ring, as the range from Cassini to the rings decreased from 236,000 km to 111,000 km. VIMS was operated in its IR-high-resolution mode (90) with a corresponding radial resolution that varies from 116 km px^{-1} in the inner C ring to 62 km px^{-1} at the F ring. Simultaneous observations were obtained with the VIMS Visible channel (VIS), operating in its nominal (or low-resolution) mode with a radial resolution that varies from 120 to 60 km px^{-1} .

On Rev 287, the aim point moved inwards from the F ring to the C ring, with the range to the rings decreasing from 194,000 km to 117,000 km. The corresponding IR radial resolution varies from 79 km px^{-1} in the outer A ring to 52 km px^{-1} in the inner C ring. Simultaneous observations were obtained with VIS, this time operating in its high-resolution mode with a radial resolution that steadily improves from 32 to 20 km px^{-1} .

A difference between the sunlit scans on Revs 262 and 287 is their azimuthal location relative to the sub-solar point on the rings: the former was made at an average solar hour angle (i.e.,

local time) of ~ 11 hrs, where saturnshine on the rings is a maximum, whereas the latter was obtained at ~ 4.5 hrs, with much less scattered light from the planet. This affects some features in the C ring spectra.

Although VIMS usually operates as an imaging spectrometer, it does this via an internal 2D scanning mirror (6). Typical frame times are several minutes, even for bright targets. In order to avoid the substantial distortion and smear that would have resulted from the rapidly-changing geometry near periapse on these orbits, the instrument was instead placed in LINE mode. In this whisk-broom mode, the scanning mirror moves in only 1 direction, producing a sequence of 64-pixel long lines painted on the target in a diagonal direction (91). As the instrument's boresight moved across the rings, the result was a single, very long, narrow image (a noodle) spanning the entire ring system.

For all lit-side observations, integration times were 160 ms per pixel for the IR channel and 5.1 s per line for the VIS channel and the scan-line length was 64 pixels. The interval between successive lines was 10.9 s, which together with the projected velocity of the aim point across the rings of $7\text{--}9 \text{ km s}^{-1}$, sets the radial interline spacing of 75–95 km in the noodles. Smear in the IR observations amounts to only ~ 1.3 km but for the visible channel it is ~ 40 km at an integration time of 5 sec per line, slightly larger than the VIS high-resolution pixel size.

With the exception of the scan on Rev 255, all observations were executed as planned and successfully returned data. On Rev 255, a problem at the Deep Space Network tracking station resulted in the central half of the scan, between the middle B ring and the inner A ring, being lost. We therefore only analyze the complete lit-side scans on Revs 262 and 287.

Image processing: In order to convert the raw line-mode data into color images such as those in Fig. 5, we followed the following steps. Individual lines were first converted to I/F spectra using the standard VIMS pipeline calibration procedure (92), modified to use a refined background correction specific to noodle mode. As described above, individual lines were then

assembled into a single noodle image with no geometric corrections or re-interpolation. A standard de-spiking algorithm was employed to remove charged-particle and γ -ray hits from Cassini's radioactive power units. A color composite version of the image was then created using wavelengths of 2.02 μm (red), 1.78 μm (green), and 1.27 μm (blue), chosen to emphasize the variations in the IR spectrum across the rings. The red channel corresponds to the center of a strong water ice absorption band, while the blue channel corresponds to a much weaker water ice band. The green channel is a continuum wavelength. Finally, a square-root histogram stretch was applied to the data in order to emphasize variations in the fainter parts of the rings, especially the inner C ring, at the expense of the bright B ring.

For the Rev 262 data, we inserted an additional filtering step using the Minimum Noise Fraction algorithm (93) in order to remove a linear trend in color across the rings; no such trend was seen in the Rev 287 data. This had the effect of removing a bluish tone in the C ring and making the two noodle images more similar in overall color.

Spectral processing: To produce the plots of spectral parameters in Fig. 6 and Figs. S9–S11, we again started with the raw line-mode data, background-subtracted to remove instrumental dark current and thermal background, and first applied the standard VIMS flux calibration (92) to convert the measured counts to ring reflectivity, expressed as I/F . A despiking algorithm was then applied to remove charged-particle hits. The calibrated observations were geometrically navigated using the appropriate Cassini SPICE kernels (94) to predict the locations of various standard ring features in the individual line-mode images, based on the feature radii of (95). After any necessary small adjustments were made to the predicted pointing, the radius of each pixel was calculated, taking into account a known offset of ~ 2 pixels between the pointing of the IR and VIS channels.

The I/F spectra for all pixels were then sorted by ring radius and grouped into a uniform set of bins at 20 km intervals, and eventually used to calculate an average spectrum for each

bin. With 3500 radial bins across 70,000 km and a total of 708 64-pixel lines across the rings, an average of ~ 12 pixels contributed to the final average spectrum for each bin. Selected small groups of spectral channels were then used to calculate band depths for each radial bin, focussing on the water ice bands at 1.55 and 2.0 μm and the spectral peak at 3.6 μm .

Water-ice band depths D_B are calculated using the standard formula (96):

$$D_B = 1 - \frac{S(\lambda_0)}{S(\text{ref})}, \quad (\text{S3})$$

where $S(\lambda_0)$ is the I/F at the bottom of the band and $S(\text{ref}) = [S(\lambda_1) + S(\lambda_2)]/2$ is an average of the I/F values at reference wavelengths on either side of the band. Typically, we use the mean of 3–6 adjacent spectral channels to evaluate $S(\lambda_i)$, while avoiding known ‘hot’ channels.

The strengths of the water ice bands measured here, including the height of the peak at 3.6 μm , are sensitive to both the level of non-icy contamination within the water ice grains and to the regolith grain size, either of which can affect the path length of photons through the water ice (97). The band depths can also be affected by inter-particle scattering, which is chiefly important at high phase angles because of the strongly-backscattering nature of the ring particles’ phase function (62).

The Visible channel data were processed in essentially the same manner, though the longer integration time means that these data are somewhat smeared in radius compared with the IR data (see above). In this wavelength region the derived spectral indicators are slopes rather than band depths. Following (57), we define the 0.35 – 0.55 μm slope (referred to by some authors as the blue slope) as

$$0.35 - 0.55 \mu\text{m slope} = 1 - \frac{S(0.35)}{S(0.55)}, \quad (\text{S4})$$

where $S(0.35)$ and $S(0.55)$ are the I/F values at 0.35 μm and 0.55 μm , respectively, as calculated from a linear fit to this spectral interval. We define the 0.55 – 0.85 μm slope (referred to

by some authors as the red slope) as

$$0.55 - 0.85 \mu\text{m slope} = \frac{S(0.85)}{S(0.55)} - 1, \quad (\text{S5})$$

where $S(0.55)$ and $S(0.85)$ are the fitted I/F values at $0.55 \mu\text{m}$ and $0.85 \mu\text{m}$, respectively. The $0.55 - 0.85 \mu\text{m}$ slopes are generally close to zero and show relatively little variability across the rings, so are omitted from Fig. S10

Supplementary Text

Interpretation and discussion for images of the main rings

It was previously known that several ring properties are altered not only within the largest density waves in Saturn's rings but also in the regions surrounding them (33, 51–53, 57). The occurrence of propellers is among these properties, as they are missing from the halo regions surrounding the strongest density waves (15).

We find that, for moderately-sized density waves such as Prometheus 9:8 (Figs. 1c and S1, Table S1), propellers are present not only in the regions surrounding the wave but also in the innermost and outermost portions of the wave itself, though they are missing from the central part of the wave. A straightforward interpretation is that there are processes in the central parts of density waves that either destroy propellers or make them less visible, and that these effects extend far beyond the wave itself for the strongest waves but do not even extend to the margins of the wave for moderately-sized waves.

Furthermore, the size distribution of the propellers is perturbed in the regions on the margins of the wave, where they are present.

The most diagnostic measure of propeller size is Δr , which has a linear relation to the size of the moonlet causing the propeller-shaped disturbance (23). This quantity is plotted in

Fig. S1c, for propellers identified in image N1871322544. In unperturbed ring regions within this image, the propeller population is dominated by values of Δr between 0.15 km and 0.4 km, with smaller numbers of propellers that are respectively larger and smaller than that range. This is especially true in the regions outward of 129,070 km, where larger numbers make the statistics more robust. However, in the innermost regions of the Prometheus 9:8 density wave, larger propellers are more numerous than medium-sized propellers, and smaller propellers are absent. Conversely, in the outermost regions of the same wave, smaller propellers are nearly as numerous as medium-sized propellers, and larger propellers are nearly absent.

Interpretation and discussion for UVIS occultations and related models

For Plateau P1 we find the height-to-wavelength ratio of the clumps to be $H/\lambda \sim 0.015$, an average width-to-wavelength ration of $W/\lambda \sim 0.039$, and an average optical depth of the gaps of $\tau_{\text{gap}} \sim 0.001$, where H is the vertical thickness of the ring, W is the average width of the gaps, S is the average separation of the gaps and $\lambda = W + S$ is the radial wavelength of the gap pattern. This model is in contrast with the self-gravity wake parameters of the A and B rings, where the narrow features are opaque clumps. This difference indicates that a different mechanism is creating the low optical depth regions, perhaps by perturbations from particularly massive ring particles (31). Model-derived optical depths which produced these best-fitting parameters and optical depths measured by the UVIS stellar occultations of Plateau P1 are compared in Fig. S5. Combining the best-fitting model parameters with the autocorrelation length in P1 from occultation optical depth profiles, $\lambda \sim 695$ m gives $S \sim 668$ m, $W \sim 27$ m, and $H \sim 11$ m.

Temperature difference between the lit and unlit sides

Figure S8 shows temperature variations across the ring plane as a function of optical depth. The lit-side temperature is greater than the unlit-side temperature for all points in the rings. The

temperature difference overall increases with optical depth, as little sunlight reaches the unlit side of optically thick rings.

The temperature differences between the lit and unlit sides of the inner A ring (from 122,000 km to 124,000 km from Saturn's center) are larger than those for the inner B ring (from 92,000 km to 99,000 km from Saturn's center) although the optical depths of these two regions are similar to each other. This regional difference has many possible causes, including the different particle size distributions, vertical dynamics, differences in Saturn heating, and differences in self-gravity wakes. Occultations of Cassini's radio signal, as measured from Earth, revealed that the size distribution of the inner A ring is narrower than that for the B1 ring (39). This means that small particles are more abundant in the latter region. Spins of small particles are expected to be fast (98). Fast rotators tend to reduce the temperature difference across the ring (84).

For optically thin rings (the C ring and the Cassini Division), the higher lit-side temperatures than the unlit-side temperatures could be caused by the fact that the phase angles for the lit side are lower than those for the unlit side. Models indicate that the phase dependence of temperature is dependent on particle spin, with small fast rotators tending to reduce the phase dependence (84). If so, then a higher abundance of small fast rotators in the C ring, compared to the Cassini Division, could account for the relatively smaller temperature differences in the C ring.

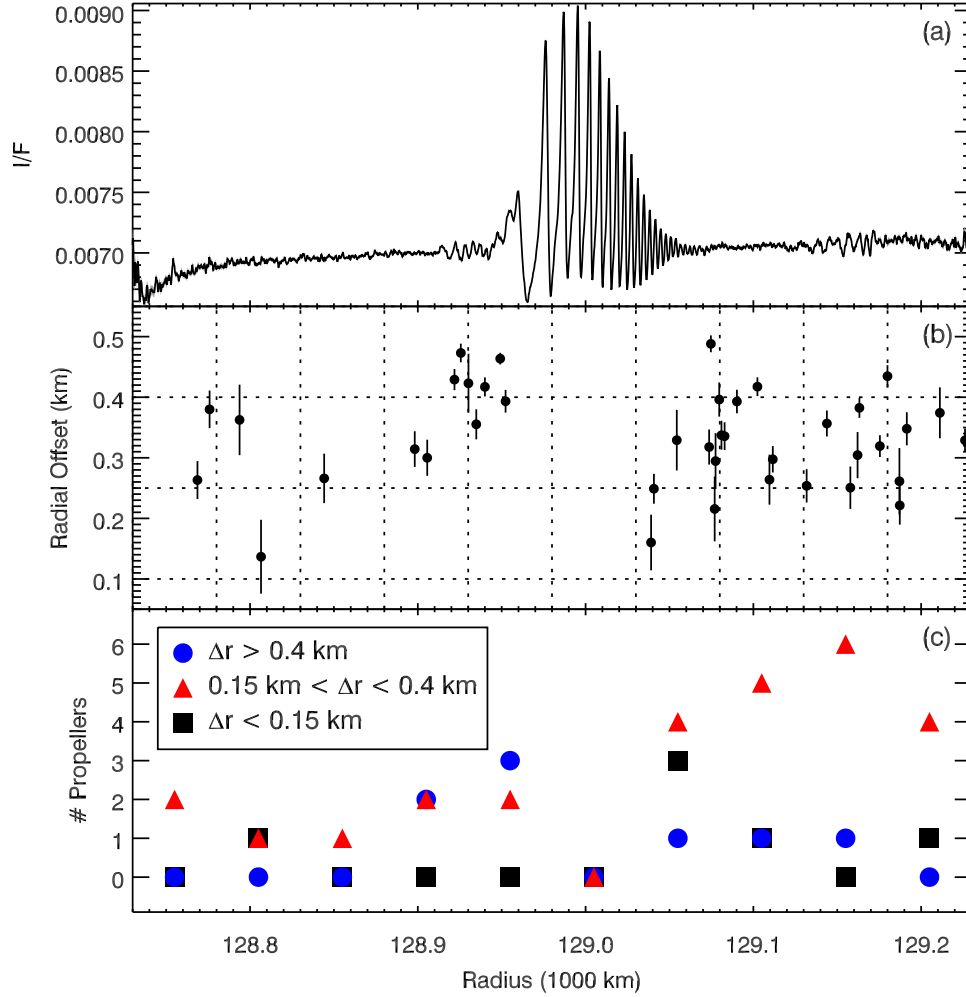


Figure S1: **Population statistics in the Propeller Belts.** (a) Radial profile of image N1871322544 (Fig. 1c), including the Prometheus 9:8 spiral density wave between approximately 128,940 and 129,070 km. (b) Size of propellers identified in image N1871322544, in terms of the radial offset Δr (Table S1). Dotted horizontal and vertical lines indicate the bins in size and location (respectively) used to generate the following plot. (c) Number of propellers belonging to each of three bins in size (see legend) at each bin in location.

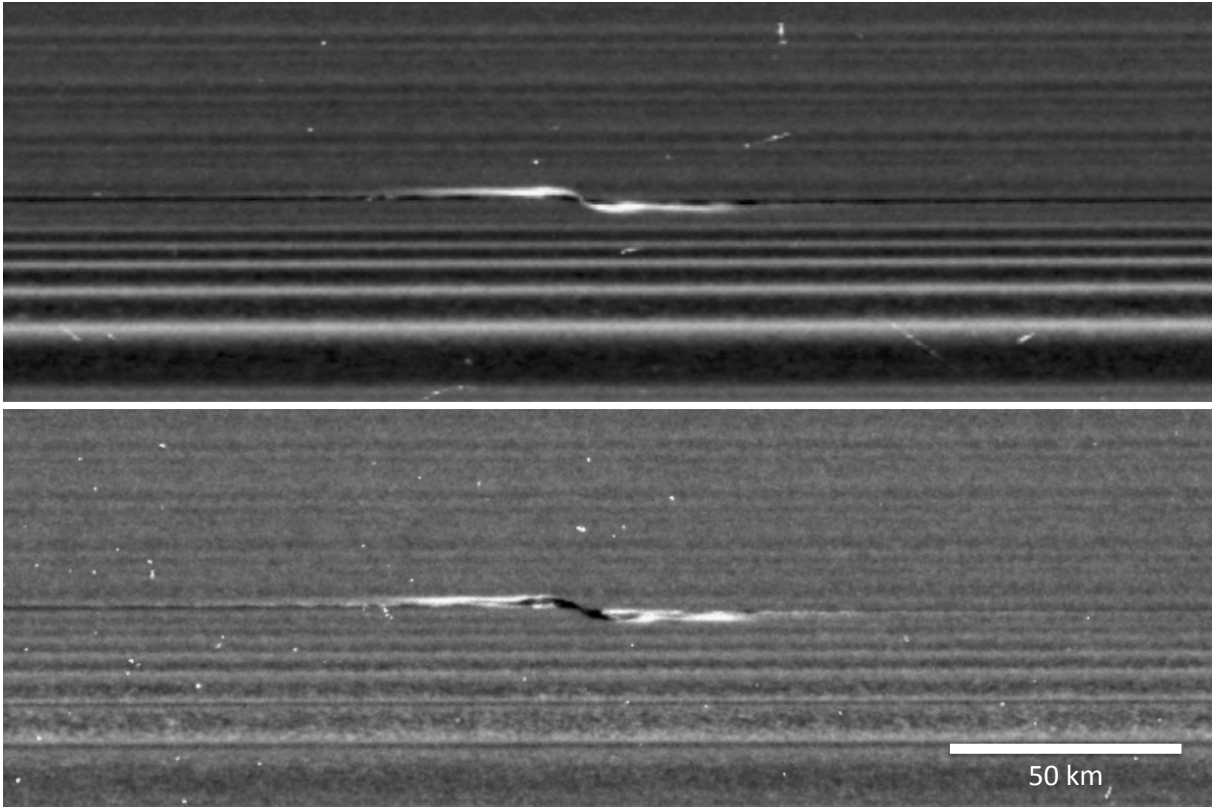


Figure S2: **Two sides of the same propeller.** Reprojected versions of images (a) N1866363047 and (b) N1866370342, showing the propeller Santos-Dumont on the lit and unlit sides of the rings, respectively. The unreprojected resolutions of the images are 0.53 and 0.41 km px^{-1} , respectively. They have been reprojected to the same resolution, for comparison.

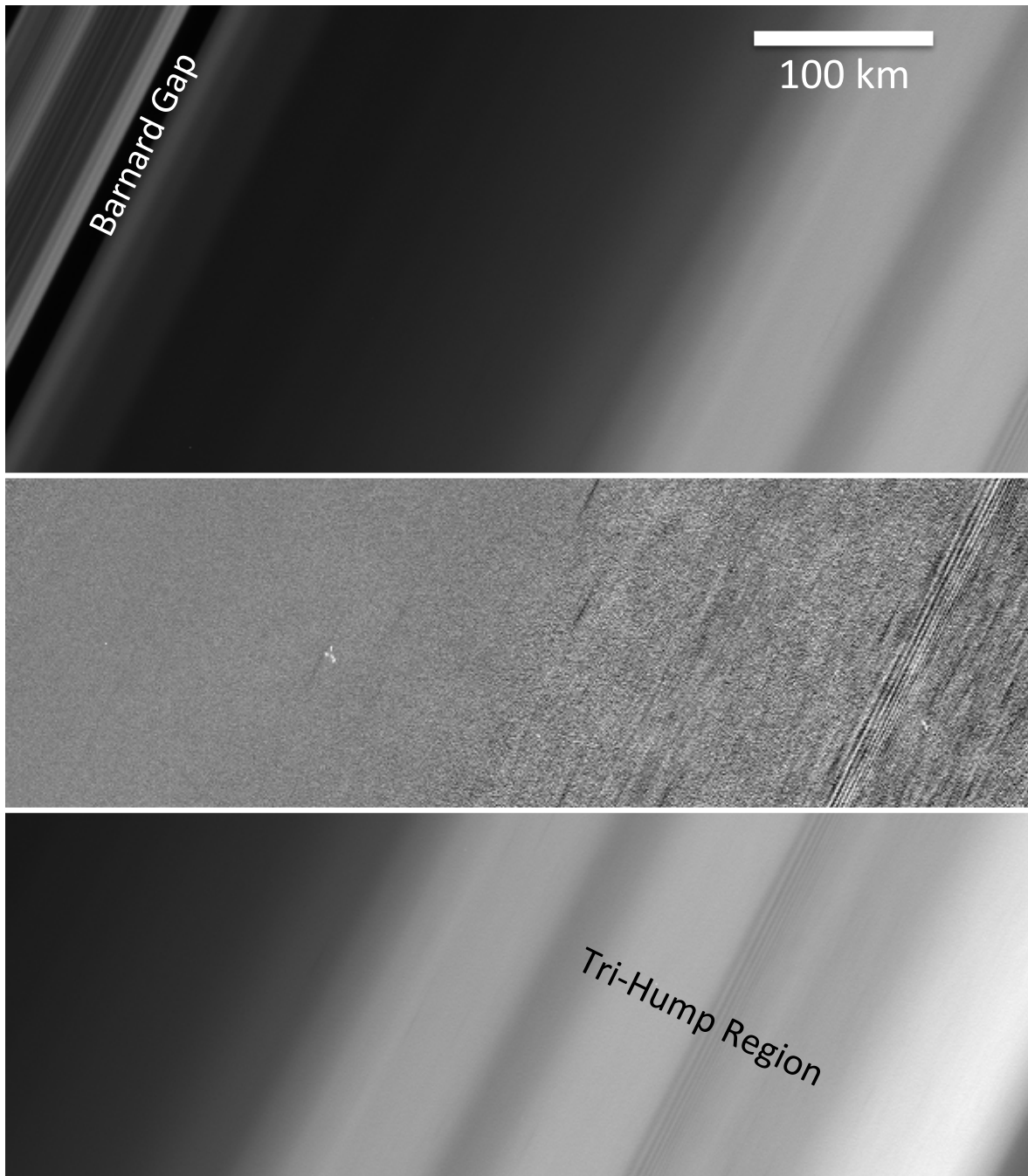


Figure S3: **Belts of textures in the outer Cassini Division.** A portion of image N1862642699, showing locations in the outer Cassini Division on the lit side of the rings at 0.69 km px^{-1} . As in Fig. 2, a strip through the middle has been filtered by subtracting the average radial profile of the image, so that local structures and textures are more visible.

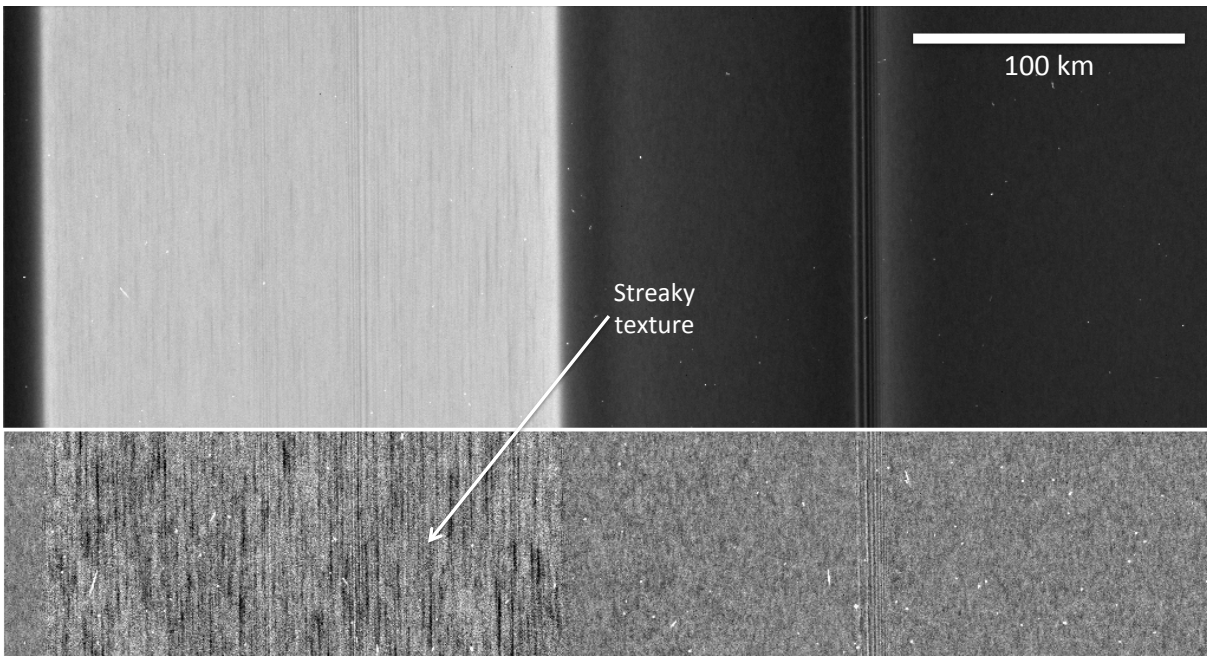


Figure S4: **Textures in the C ring.** A portion of image N1874678736, showing Plateau P5 in the C ring on the unlit side of the rings at 0.44 km px^{-1} . As in Fig. 2, a strip through the middle has been filtered by subtracting the average radial profile of the image, so that local structures and textures are more visible.

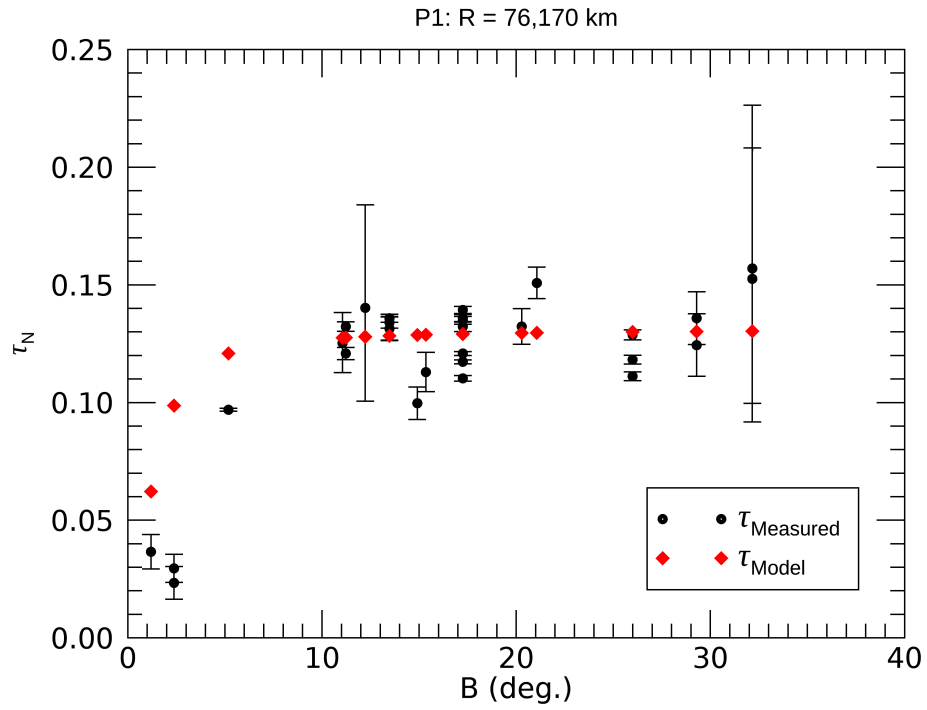


Figure S5: **Model-determined and measured UVIS normal optical depth in Plateau P1.** The results shown here minimize the reduced chi-squared statistic, $\chi^2 \sim 1.3$. The best-fitting model parameters are $H/\lambda \sim 0.015$, $W/\lambda \sim 0.039$, $\tau_{\text{gap}} \sim 0.001$, and $\tau_{\text{clump}} \sim 0.132$.

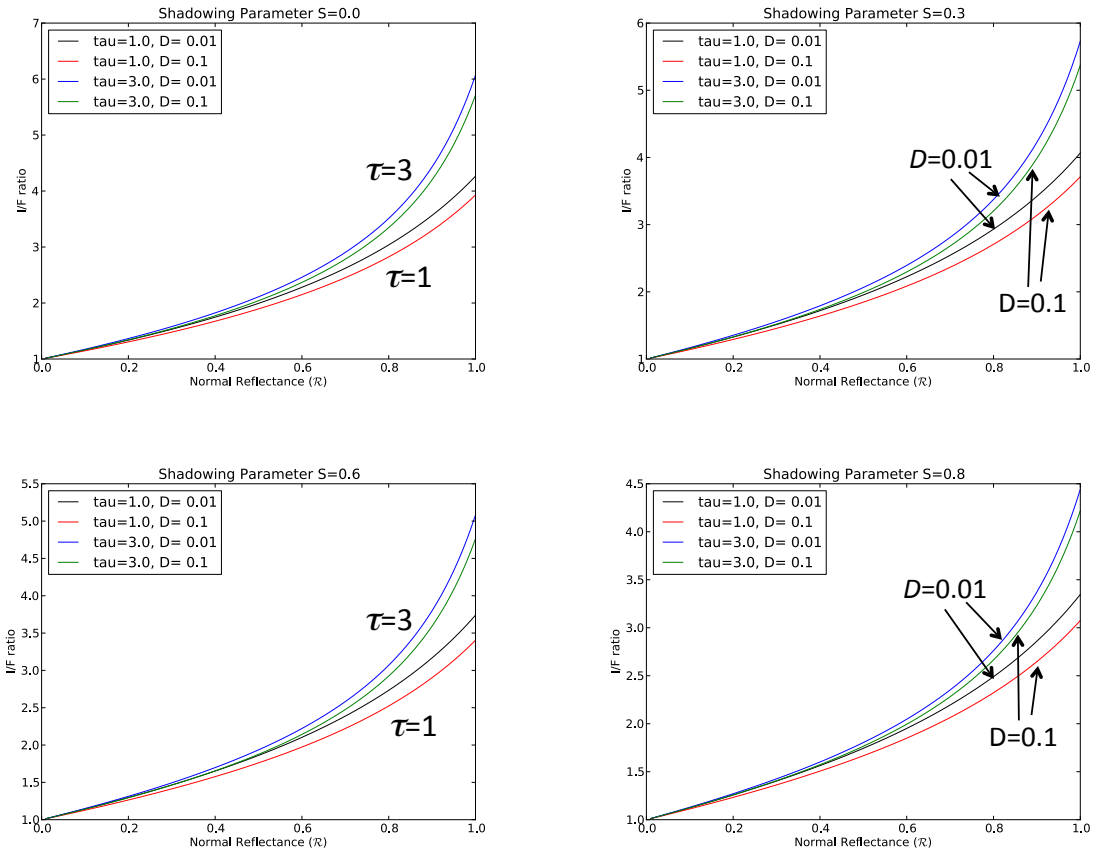


Figure S6: The four panels show the I/F ratio $R_{I/F}$, calculated at the illumination and viewing geometry of Fig. 4a (phase angle $\alpha = 111^\circ$, solar elevation angle $B' = 26^\circ$, spacecraft elevation angle $B = 41^\circ$). The normal reflectance on the horizontal coordinate (the angle-integrated reflectance of a smooth facet of the same surface material) is closely related to the particle spherical albedo (76). Each panel is for a different surface roughness/shadowing parameter S , where the ring particles are in the range of $S = 0.8$, depending on wavelength (43). The curves are labeled by their optical depth τ and particle volume density D .

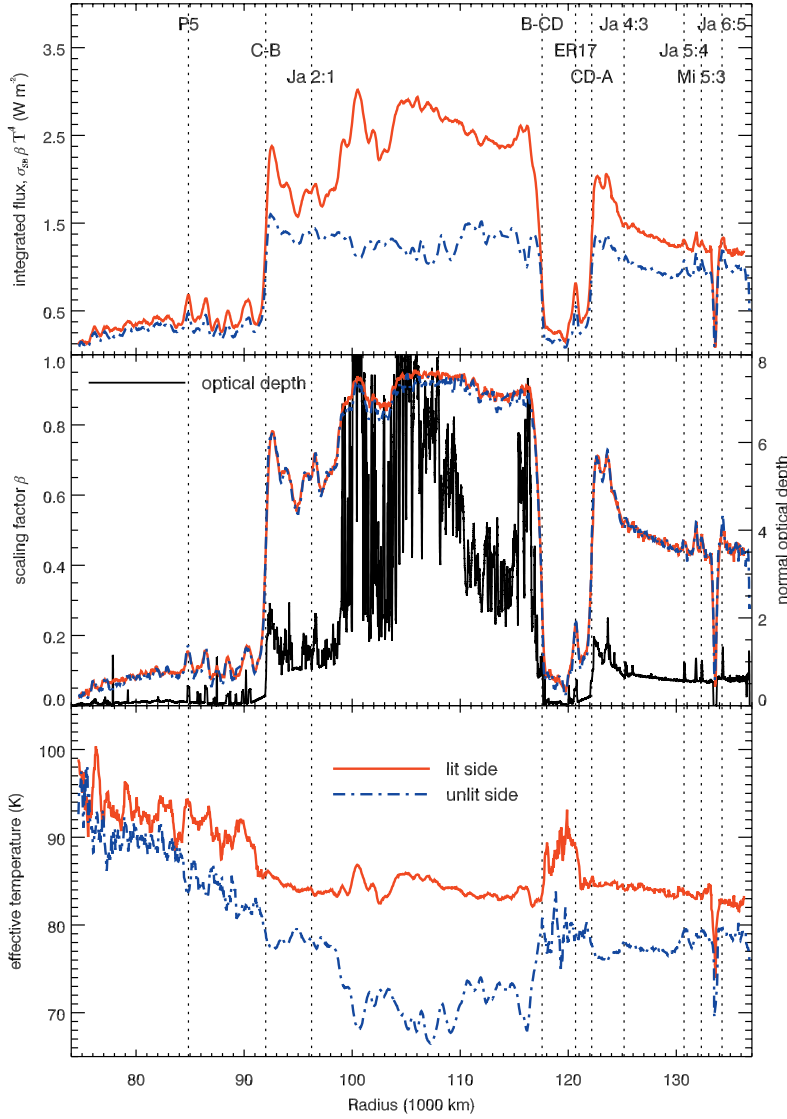


Figure S7: **Radial profiles of thermal infrared properties.** Data from the CIRS lit (red) and unlit-side (blue) scans on Rev 262. The upper panel shows the integrated flux $\sigma_{\text{SB}}\beta T^4$, where σ_{SB} is the Stefan-Boltzmann constant, with the vertical dotted lines indicating the locations of the ring boundaries, the strongest density waves, and two prominent features in the C ring and the Cassini Division (plateau P5 and the tri-hump region ER17). The middle panel shows the scaling factor β along with a normal optical depth profile obtained from a UVIS occultation of the star β Centauri on Rev 077, smoothed at a radial resolution of 10 km. The bottom panel shows the effective temperature T . β and T are simultaneously obtained from fitting the Planck function, see Eq. S2.

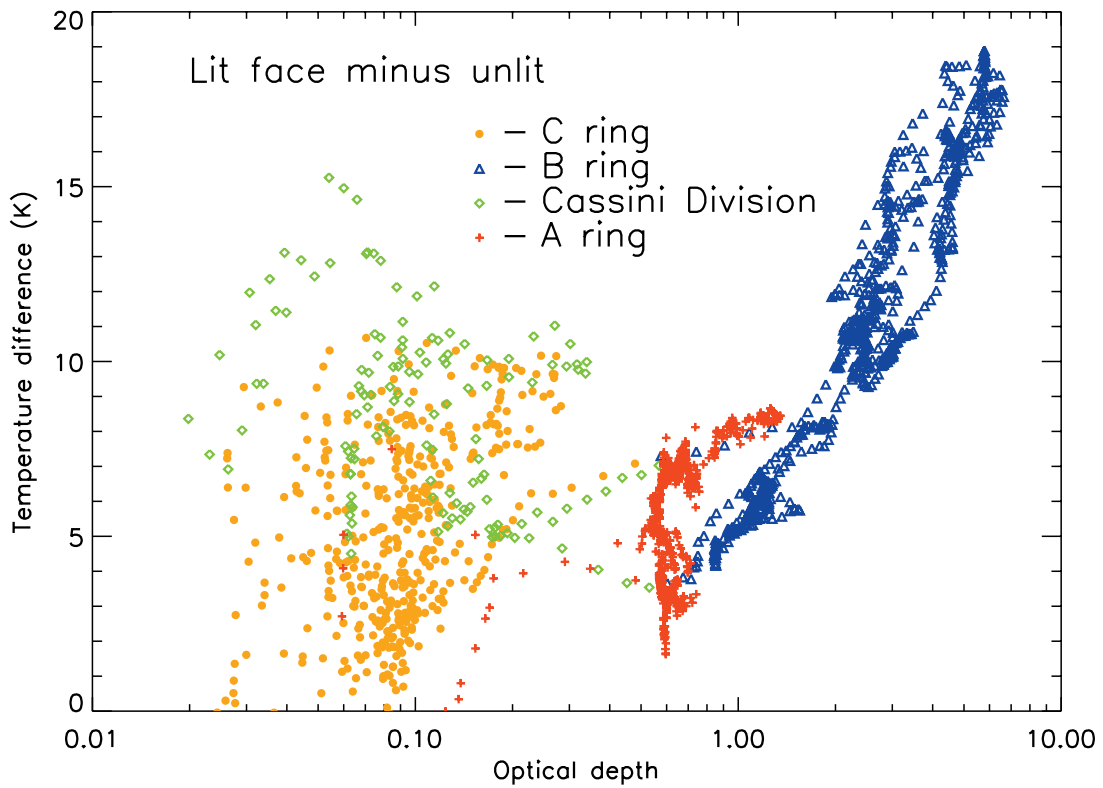


Figure S8: **Temperature difference across the ring plane.** Data plotted as a function of optical depth. Individual rings are identified by color: A ring in red (plus signs); B ring in blue (triangles); C ring in orange (filled circles); Cassini Division in green (diamonds).

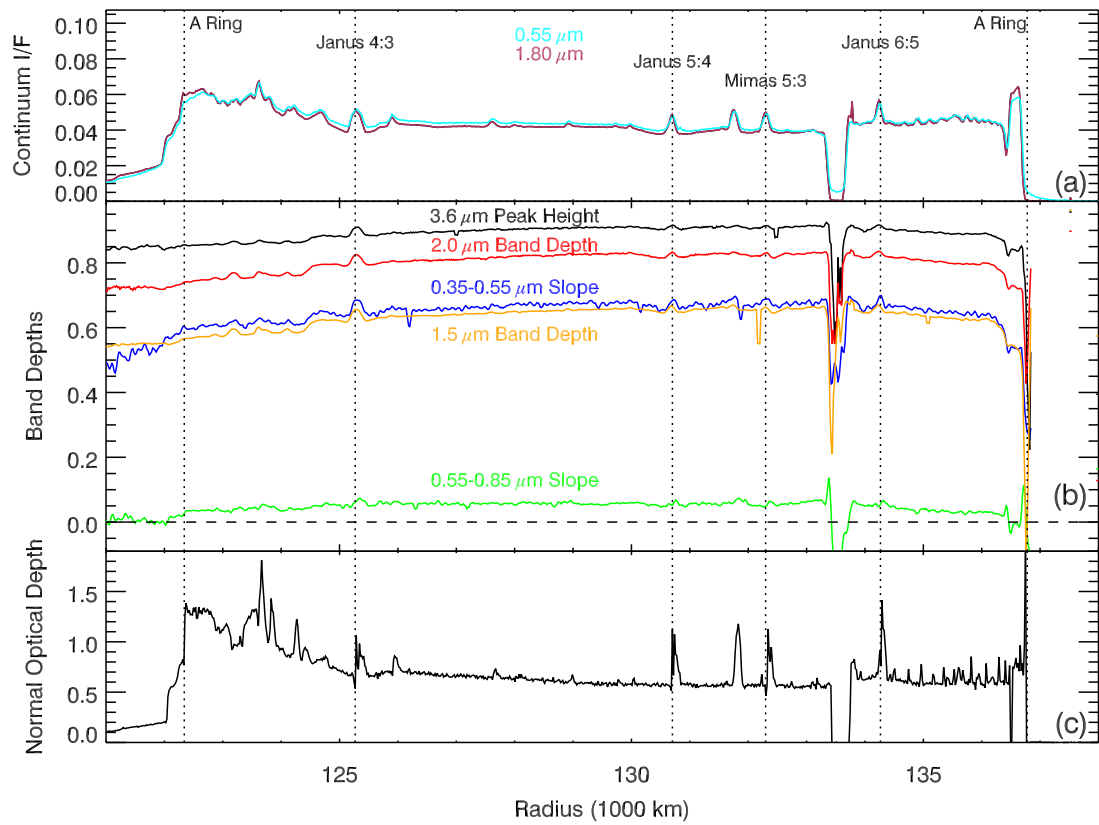


Figure S9: **Radial profiles of spectral parameters: A ring.** As in Fig. 6, but zoomed to show the vicinity of the A ring.

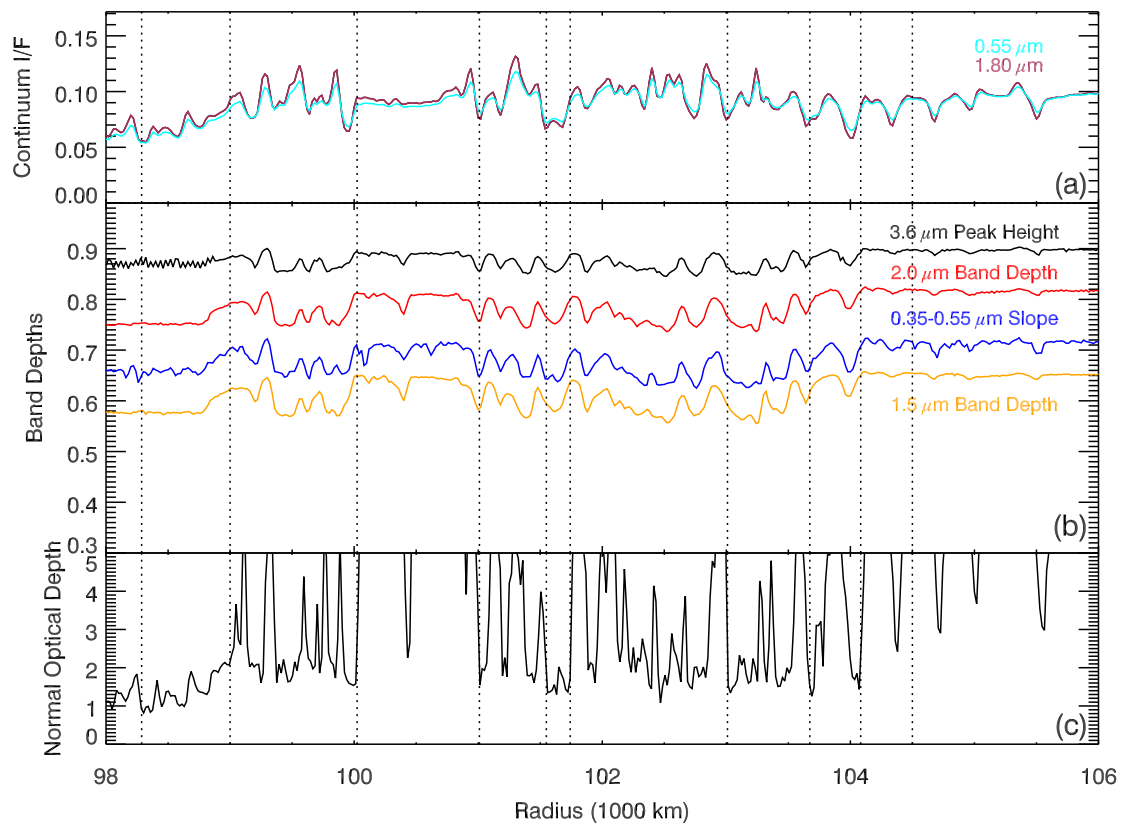


Figure S10: **Radial profiles of spectral parameters: B2 ring region.** As in Fig. 6, but zoomed to show the B2 region of the B ring (the same region covered in Fig. 4a). The green curve ($0.55 - 0.85 \mu\text{m}$ slope) is omitted because it is essentially zero and therefore off-scale.

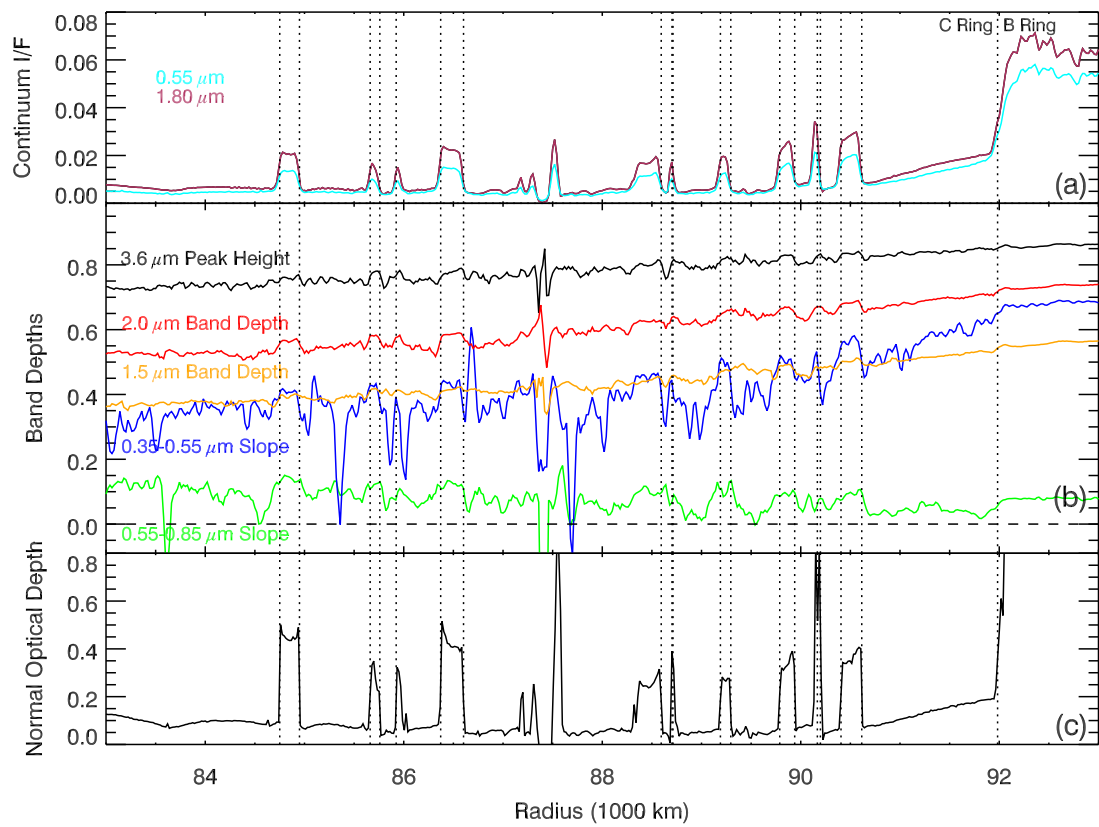


Figure S11: **Radial profiles of spectral parameters: outer C ring.** As in Fig. 6, but zoomed to show the vicinity of the outer C ring.

Table S1: Locations and fitted parameters for reported propellers. The format of Name is Orbit-Num-Letter, where Orbit and Num identify the image (in this case the image N1871322544, shown in Fig. 1c, is the 8th image of the high-resolution observation taken during Rev 270), and Letter identifies the feature within the image. Details of the model and parameters are as previously published (15). Selected parameters in this table are plotted in Fig. S1.

Name	Image	[line, sample]	Radius (km)	Longitude (°)	α (km)	b (km)	$\Delta\ell$ (km)	Δr (km)
270-008-A	N1871322544	[13.7, 944.4]	128952.31±0.39	344.39286±0.00017	1.570±0.043	0.628±0.020	3.090±0.046	0.393±0.019
270-008-B	"	[24.1, 261.0]	129175.40±0.39	344.33029±0.00017	1.607±0.043	0.601±0.016	3.010±0.044	0.319±0.018
270-008-C	"	[35.3, 100.1]	129226.14±0.39	344.31432±0.00017	1.878±0.054	0.607±0.019	3.317±0.056	0.329±0.019
270-008-D	"	[55.7, 478.5]	129097.53±0.39	344.34511±0.00018	0.876±0.062	0.790±0.062	-1.646±0.066	0.117±0.064
270-008-E	"	[60.8, 130.3]	129211.17±0.39	344.31331±0.00018	1.101±0.058	0.727±0.042	1.969±0.060	0.374±0.042
270-008-F	"	[61.0, 438.7]	129109.59±0.39	344.34079±0.00018	1.065±0.069	0.584±0.042	2.210±0.073	0.264±0.041
270-008-G	"	[64.9, 535.4]	129076.96±0.39	344.34886±0.00018	0.921±0.083	0.505±0.050	2.020±0.088	0.216±0.054
270-008-H	"	[81.3, 322.6]	129143.83±0.39	344.32749±0.00018	1.277±0.040	0.635±0.020	2.939±0.042	0.357±0.021
270-008-I	"	[85.0, 264.8]	129162.11±0.39	344.32181±0.00018	1.306±0.066	0.692±0.037	2.142±0.065	0.304±0.038
270-008-J	"	[94.0, 183.0]	129187.26±0.39	344.31320±0.00018	1.175±0.052	0.644±0.031	2.382±0.055	0.221±0.032
270-008-K	"	[102.2, 165.3]	129191.45±0.39	344.31044±0.00018	1.159±0.053	0.596±0.032	2.909±0.054	0.348±0.027
270-008-L	"	[161.8, 997.0]	128905.58±0.39	344.37608±0.00018	1.595±0.068	0.645±0.029	2.596±0.067	0.300±0.030
270-008-M	"	[168.6, 432.9]	129090.19±0.39	344.32468±0.00017	1.677±0.044	0.684±0.020	3.117±0.045	0.393±0.019
270-008-N	"	[175.6, 207.1]	129163.19±0.39	344.30353±0.00017	1.654±0.047	0.558±0.021	3.218±0.050	0.382±0.017
270-008-O	"	[219.2, 197.3]	129157.79±0.39	344.29635±0.00018	0.887±0.052	0.535±0.031	2.199±0.054	0.251±0.035
270-008-P	"	[224.4, 910.1]	128921.83±0.39	344.35923±0.00017	1.797±0.047	0.633±0.018	4.108±0.049	0.429±0.017
270-008-Q	"	[242.6, 887.6]	128925.65±0.39	344.35458±0.00017	2.209±0.050	0.625±0.014	4.095±0.051	0.473±0.015
270-008-R	"	[260.6, 960.1]	128898.18±0.39	344.35845±0.00018	1.366±0.060	0.607±0.027	2.301±0.060	0.314±0.030
270-008-S	"	[314.9, 218.9]	129131.76±0.39	344.28440±0.00018	1.164±0.050	0.586±0.027	2.452±0.053	0.254±0.027
270-008-T	"	[323.8, 367.7]	129080.99±0.39	344.29637±0.00018	1.595±0.058	0.590±0.021	3.311±0.061	0.337±0.024
270-008-U	"	[350.9, 286.4]	129102.43±0.39	344.28519±0.00017	1.774±0.041	0.626±0.016	3.495±0.043	0.417±0.016
270-008-V	"	[353.7, 372.0]	129073.64±0.39	344.29241±0.00018	1.153±0.050	0.606±0.030	2.327±0.053	0.318±0.029
270-008-W	"	[375.9, 14.4]	129187.07±0.39	344.25739±0.00018	1.044±0.089	0.582±0.056	1.929±0.093	0.261±0.055
270-008-X	"	[385.2, 788.2]	128930.16±0.39	344.32498±0.00018	1.222±0.083	0.667±0.051	2.160±0.085	0.423±0.049
270-008-Y	"	[396.0, 24.0]	129179.94±0.39	344.25532±0.00017	1.812±0.051	0.588±0.017	3.528±0.053	0.435±0.018
270-008-Z	"	[410.0, 320.0]	129079.66±0.39	344.27962±0.00018	1.679±0.076	0.623±0.031	3.265±0.073	0.396±0.028
270-008-a	"	[459.4, 413.6]	129039.02±0.39	344.28079±0.00018	1.223±0.073	0.774±0.043	1.681±0.061	0.160±0.046
270-008-b	"	[477.0, 286.4]	129077.48±0.39	344.26691±0.00018	0.867±0.060	0.625±0.049	1.924±0.063	0.295±0.046
270-008-c	"	[484.4, 714.5]	128934.83±0.39	344.30400±0.00018	1.528±0.059	0.586±0.022	2.490±0.058	0.355±0.025
270-008-d	"	[577.6, 642.9]	128940.00±0.39	344.28408±0.00017	1.706±0.037	0.669±0.016	3.280±0.038	0.417±0.016
270-008-e	"	[618.8, 313.0]	129040.70±0.39	344.24870±0.00018	1.492±0.054	0.612±0.026	2.889±0.057	0.249±0.025
270-008-f	"	[640.9, 84.8]	129111.57±0.39	344.22522±0.00017	1.997±0.059	0.684±0.021	3.194±0.057	0.298±0.022
270-008-g	"	[667.3, 993.6]	128806.56±0.39	344.30234±0.00018	0.961±0.088	0.592±0.056	1.576±0.087	0.137±0.061
270-008-h	"	[697.0, 861.8]	128844.17±0.39	344.28627±0.00018	1.395±0.080	0.647±0.040	2.284±0.080	0.266±0.041
270-008-i	"	[744.3, 515.5]	128949.11±0.39	344.24851±0.00017	2.359±0.033	0.619±0.009	4.457±0.034	0.464±0.010
270-008-j	"	[778.4, 114.4]	129074.69±0.39	344.20791±0.00017	2.079±0.044	0.625±0.013	3.344±0.043	0.488±0.014
270-008-k	"	[833.4, 932.9]	128793.74±0.39	344.27278±0.00018	1.002±0.097	0.583±0.056	1.668±0.090	0.363±0.058
270-008-l	"	[865.9, 123.7]	129054.37±0.39	344.19605±0.00018	1.200±0.073	0.747±0.048	1.960±0.072	0.329±0.050
270-008-m	"	[873.0, 985.3]	128768.63±0.39	344.27169±0.00018	1.715±0.072	0.681±0.029	2.735±0.070	0.263±0.031
270-008-n	"	[896.3, 19.2]	129082.84±0.39	344.18238±0.00018	1.943±0.068	0.598±0.022	3.186±0.068	0.336±0.023
270-008-o	"	[946.6, 919.4]	128775.86±0.39	344.25510±0.00018	1.361±0.055	0.701±0.032	2.352±0.056	0.380±0.031

Table S2: **Geometry data of CIRS radial scans.** Date is year and day of year, Rings is the rings covered by each scan, δa is the radial extent of the footprint projected on the ring plane, B' is the solar elevation angle, B is the spacecraft elevation angle, α is the phase angle, L is the local hour angle of ring particles around Saturn with the origin at the midnight, $L_{S/C}$ is the spacecraft local hour angle around the footprint, and $R_{S/C}$ is the spacecraft distance from the ring in units of Saturn's equatorial radius, R_{Sat} . All the values are mean values for each scan.

Scan	Date	Rings	δa (km)	B' (degs)	B (degs)	α (degs)	L (degs)	$L_{S/C}$ (degs)	$R_{S/C}$ (R_{Sat})
Lit face									
L262	2017-052	C, B, CD	795	26.70	71.09	62.06	179.64	98.65	3.39
L268	2017-095	A	363	26.72	78.86	56.00	182.23	140.22	1.63
Unlit face									
U262	2017-052	C, B, CD	632	26.70	-74.64	128.84	227.55	325.00	2.78
U268	2017-095	A	338	26.72	-82.89	120.95	212.27	260.51	1.47

Table S3: **Names of prominent features and their locations.** Widths are also shown for plateaux. The data for the plateaux are from (66). The data for the density waves are from (99). The location of the bending wave is from (100).

Name	location (km)	width (km)
P1	76188	155
P2	77085	150
P3	77378	65
P4	79243	45
P5	84850	200
P6	85708	95
P7	86490	230
P8	88473	245
P9	89865	105
P10	89863	150
P11	90508	205
ER17	120675	250
Janus 4:3 DW	125266	
Janus 5:4 DW	130700	
Mimas 5:3 BW	131898	
Mimas 5:3 DW	132295	
Janus 6:5 DW	134264	

Table S4: **List of VIMS ring spectral observations during the RGO and GF orbits.** Geometric data for VIMS radial scans. Obs_ID is the Cassini observation identifier. The date is given as year and day of year, Dur is the observation duration, including turns, and Range is the distance of Cassini from the ring target. B and α are the spacecraft elevation angle and phase angle at the observation point, which are constant across each scan. Dir'n specifies the direction of the scan across the rings: inwards or outwards, and H.A. is the (range of) local hour angles observed, where 0h = midnight and 12h = noon. v_{rad} is the projected velocity of the VIMS pixel across the rings, in the radial direction. Pixels indicates the length of each scan line, t_{line} the duration of a scan line, and Lines the total number of lines in the scan. Δr is the average radial spacing between successive lines.

Obs-ID	Date (year-day)	Dur. (h:mm)	Range (10^3 km)	B (deg)	α (deg)	Dir'n	H.A. (hr)	v_{rad} (km/s)	pixels	t_{line} (sec)	Lines	Δr (km)
VIMS-255RI-COMPLITB	2017-002	3:00	212-80	73	56	out	10-12	7.0	64	10.9	512	76
VIMS-260RI-COMPDRK	2017-038	2:30	111-209	74	129	in	~ 15	-7.0	32	5.7	1318	40
VIMS-262RI-COMPLITB	2017-052	3:00	236-111	71	62	out	10-12	7.0	64	10.9	935	76
VIMS-262RI-COMPDRK	2017-052	2:30	104-199	74	129	in	~ 14	-7.0	32	5.7	1483	40
VIMS-287RI-COMPLITB	2017-219	2:53	194-117	80	73	in	3-6	-8.9	64	10.9	708	95